Check for updates

ADVANCING EARTH AND SPACE SCIENCES

JGR Space Physics

RESEARCH ARTICLE
10.1029/2024JA033161

Electron Phase Space Densities in Geostationary Orbits as Measured With GK2A, GOES-16, and GOES-17 Satellites

C. H. Lee[1], J. Seon[1], W. H. Seol[2], K. H. Kim[1], D. E. Larson[3], G. K. Parks[3], H. U. Auster[4], W. Magnes[5], S. Kraft[6], D. Y. Lee[7], A. Boudouridis[8,9], P. T. M. Loto'aniu[8,9], and J. V. Rodriguez[8,9]

[1]School of Space Research, Kyung Hee University, Yongin, Republic of Korea, [2]Korea Astronomy and Space Science Institute, Daejeon, Republic of Korea, [3]Space Science Laboratory, University of California, Berkeley, CA, USA, [4]Institute of Geophysics and Extraterrestrial Physics, Technische Universität Braunschweig, Braunschweig, Germany, [5]Austrian Academy of Sciences, Space Research Institute, Graz, Austria, [6]European Space Operations Centre (ESOC), European Space Agency, Paris, France, [7]Department of Astronomy and Space Science, Chungbuk National University, Chungcheongbuk-do, Republic of Korea, [8]Cooperative Institute for Research in Environmental Sciences, University of Colorado, Boulder, CO, USA, [9]NOAA National Centers for Environmental Information, Boulder, CO, USA

Key Points:

- Electron phase space densities (PSDs) were computed using data from three geostationary satellites: GK2A, GOES-16, and GOES-17
- Comparisons indicate that measurements from these satellites are sufficiently consistent for assessing the radial profiles of PSDs
- The research on PSD gradients suggests a mechanism that enhances negative gradient growth during geomagnetically active periods

Correspondence to:
J. Seon,
jhseon@khu.ac.kr

Citation:
Lee, C. H., Seon, J., Seol, W. H., Kim, K. H., Larson, D. E., Parks, G. K., et al. (2025). Electron phase space densities in geostationary orbits as measured with GK2A, GOES-16, and GOES-17 satellites. *Journal of Geophysical Research: Space Physics*, *130*, e2024JA033161. https://doi.org/10.1029/2024JA033161

Received 13 SEP 2024
Accepted 19 MAR 2025

Abstract This study investigated electron phase space densities (PSDs) in geostationary orbits using data from Korea's geostationary satellite, GK2A, as well as GOES-16 and GOES-17 satellites. The PSDs were computed from electron fluxes measured by each satellite during a geomagnetically quiet period as defined by stringent conditions on geomagnetic activity. The conjunction of the satellites over invariant coordinates enabled electron PSDs from pairs of satellites to be compared to assess the extent of deviation of the PSD ratios from the expected ratio of one, as inferred from the Liouville theorem. The results show that PSDs from the satellites are sufficiently consistent to allow the estimation of the radial gradient of the PSDs. Comparisons of radial gradients estimated in this manner show that positive radial gradients prevail during geomagnetically quiet periods, whereas both positive and negative gradients may occur at similar frequencies during active periods. This study provides statistical insights into the physical mechanisms responsible for the observed radial gradient profiles based on findings from a wide range of local times during both geomagnetically quiet and active periods.

Plain Language Summary This study investigated the distribution of electrons in geostationary orbits using data from the GK2A, GOES-16, and GOES-17 satellites. These orbits are crucial for understanding the populations of charged particles in Earth's outer radiation belts, which are highly relevant to space science, weather forecasting, remote sensing, communication, and defense applications. We first assimilated the data from the satellites by computing the electron phase space density, a physical quantity expected to be conserved unless perturbed by a physical mechanism, with a characteristic time scale shorter than the periodicity of the electron's drift motion around the Earth. This data assimilation is critical because of the inherent differences in instrumentation and data processing between the GK2A and GOES satellites. After confirming the consistency of the data sets, we calculated the radial gradients of the distributions of electrons during geomagnetically quiet and active periods. Our findings indicate that positive gradients are predominant near the near-magnetic equatorial plane during quiet periods, whereas negative gradients become more frequent during active periods.

1. Introduction

The characterization and understanding of the population of charged particles in geostationary orbits have remained a highly prioritized area of research, attracting significant attention from both academic and programmatic perspectives. Geostationary orbits lie close to the central region of the Earth's radiation belt and hold immense potential benefits for a wide range of disciplines, including space physics, meteorology, remote sensing, communication, and military applications, owing mainly to their synchronization with Earth's rotation. Early space missions have firmly established that geostationary orbits are typically immersed in the outer radiation belts containing highly energetic, relativistic electrons (Arnoldy & Chan, 1969; Baker et al., 1978; Bogott & Mozer, 1973; Higbie et al., 1978; Lezniak & Winckler, 1970). Furthermore, research has demonstrated that electron populations near geostationary orbits exhibit significant variability, with order-of-magnitude flux increases and decreases, likely linked to geomagnetic storm and substorm activities. Various physical mechanisms have been proposed to explain these observed variations, encompassing both adiabatic and nonadiabatic effects,

© 2025. The Author(s).
This is an open access article under the terms of the Creative Commons Attribution-NonCommercial License, which permits use, distribution and reproduction in any medium, provided the original work is properly cited and is not used for commercial purposes.

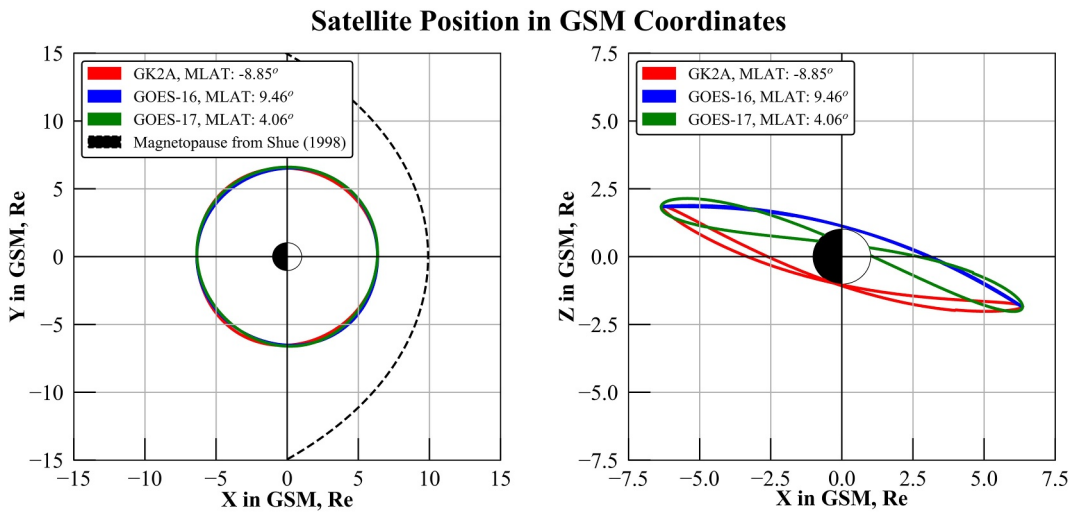

Figure 1. Positions of the three geostationary satellites in Geocentric Solar Magnetospheric (GSM) coordinates. Red, blue, and green solid lines indicate orbits of GK2A, GOES-16, and GOES-17, respectively. Black dashed line indicates the magnetopause model by Shue et al. (1998) where the input parameters are chosen arbitrarily. The magnetopause models was generated with input parameters of Bz = 0 nT and solar wind dynamic pressure (Pdyn) = 2.5 nPa. Magnetic latitudes of GK2A, GOES-16, and GOES-17 are approximately estimated as −8.9°, 9.4°, and 4.0°, respectively assuming a dipole field.

including, but not limited to, the acceleration and loss caused by the influence of radial diffusion, electromagnetic ion cyclotron waves, whistler waves, and ultralow-frequency waves. (For reviews of these processes, see Li & Hudson, 2019; Millan & Baker, 2012; Millan & Thorne, 2007; Ripoll et al., 2020).

Electron phase space densities (PSDs) in the radiation belt are often expressed in terms of conserved physical quantities that provide a useful set of coordinates. In these coordinates, the PSDs remain constant, provided that the time scales of the variations are longer than the periodicities of the associated quantities (Roederer, 1970; Roederer & Lejosne, 2018; Roederer & Zhang, 2014). Extensive analyses of observations on the outer radiation belts have been made in terms of PSD variations with the partial intent of estimating the relative role of adiabatic and nonadiabatic effects. For example, Kim and Chan (1997) estimated the contribution of the fully adiabatic effect to their observed relativistic electron fluxes by applying Liouville's theorem to equatorially mirroring particles and found that a significant fraction of the observations could be accounted for in terms of the adiabatic effect. Using pitch angle distribution (PAD) measurements, Chen et al. (2005) were able to calculate PSDs as a function of three adiabatic invariants related to the periodic motions of gyration, bouncing, and drift in the outer radiation belts and applied their method to three geostationary satellites during geomagnetically quiet times. For geomagnetically disturbed times, Chen et al. (2007) successively employed the same methodology to demonstrate the significance of local acceleration resulting from gyro-resonant interactions compared to the slower process of radial diffusion. Using measurements from the highly inclined, highly elliptical Polar spacecraft, Selesnick and Blake (2000) and Green and Kivelson (2001, 2004) derived the PSDs for relatively larger second adiabatic invariants to further validate the significance of local acceleration. These methodologies for calculating the electron PSDs subsequently allowed for inferences on the acceleration mechanism by allowing the radial profiles of PSDs to be examined (Iles et al., 2006; Kalliokoski et al., 2022; Liu et al., 2020; Miyoshi et al., 2003; Morley et al., 2013; Ozeke et al., 2019; Y. Shprits et al., 2012; Taylor et al., 2004; Turner et al., 2012, 2013, 2014).

This paper presents the findings of electron PSD calculations based on measurements obtained from three geostationary satellites: Geo-KOMPSAT-2A (GK2A) (Magnes et al., 2020; Seon et al., 2020), Geostationary Operational Environmental Satellites (GOES)-16, and GOES-17 (Boudouridis et al., 2020; Dichter et al., 2015; Kress et al., 2020; Loto'aniu et al., 2019; Rich et al., 2024). By incorporating the newly added GK2A satellite data into the existing GOES-based geostationary satellite data, this study enables a more comprehensive investigation of the electron PSD distribution in the outer radiation across a broader range of local times, with improved energy resolution. As shown in Figure 1, these satellites operate over a wide range of local time regions, specifically, at 128.2°E, 75.2°W, and 137.2°W, respectively, and allow for a comprehensive examination of electron PSDs in the outer radiation belt by simultaneously providing measurements of the local electron energy spectra and vector

21699402, 2025, 4, Downloaded from https://agupubs.onlinelibrary.wiley.com/doi/10.1029/2024JA033161, Wiley Online Library on [02/10/2025]. See the Terms and Conditions (https://onlinelibrary.wiley.com/terms-and-conditions) on Wiley Online Library for rules of use; OA articles are governed by the applicable Creative Commons License

magnetic fields. This research advances previous studies by utilizing continuous measurements of both electron energy spectra over broad energy ranges and local magnetic fields, which are critical for understanding outer radiation belt dynamics. However, simultaneous measurements of these parameters have been unavailable. For instance, the Energetic Particle Sensor on GOES-N series, which operated prior to GOES-R series (GOES-16 and GOES-17), provided electron fluxes over limited energy ranges (See National Oceanic and Atmospheric Administration, 2010), while the synchronous orbit particle analyzer on Los Alamos geostationary satellites (Belian et al., 1996) measured particle fluxes but did not sample local magnetic field vectors. In contrast, the new observations from the three geostationary satellites utilized in this study, with their more comprehensive measurements of particles and fields across a broader range of local times, are expected to offer enhanced insights into the outer radiation belts.

2. Instrumentation

GK2A is a Korean geostationary satellite located at a local time of 128.2°E. It was launched on 4 December 2018 and has been continuously monitoring energetic particles and magnetic fields since May 2019. The space weather observations aboard GK2A are performed with a suite of instruments consisting of three particle detectors (PDs) (Seon et al., 2020), a charging monitor (Woo et al., 2020), and a four-sensor Service Oriented Spacecraft Magnetometer (SOSMAG) (Magnes et al., 2020). Each PD consists of two telescopes that are mechanically configured back-to-back with a field of view (FOV) of 20° × 20° and measures electrons and ions using silicon detectors equipped with foils and magnets for the separation of ions and electrons. The six PD telescopes measure electron fluxes centered at angles of 15°, 51°, 71°, 109°, 129°, and 165° relative to the northerly direction of the Earth. For this study, the electrons measured by the PD telescopes are in the energy range of 125–2,994 keV. Within this range, 39 energy bins are allocated with the energy resolution ΔE set at 25, 50, and 100 keV for energy ranges of 125–400 keV, 400–1,400 keV, and 1,400–2,200 keV, respectively. To convert the count rates into differential fluxes, energy-dependent geometric factors were first derived from a Geant4 simulation and subsequently adjusted to best account for count rates measured during geomagnetically quiet times, assuming predetermined energy spectra (Seol et al., 2023). An additional integrated energy bin is included above 2,200 keV, following bow-tie analysis (Van Allen et al., 1974), with a best-fit energy of 2,994 keV, resulting in a total of 40 energy bins from each PD instrument. SOSMAG is a science-grade magnetometer developed by the European Space Agency with a particular design emphasis on avoiding strict magnetic cleanliness requirements for the hosting spacecraft. It employs two science-grade fluxgate sensors mounted on an approximately 1-m-long boom, along with two additional magnetoresistance sensors within the spacecraft body. The magnetometer performs automated onboard correction of dynamic stray fields generated by the spacecraft. For the present study, both the PD and SOSMAG measurements are averaged over 1-min intervals.

On the other hand, the GOES-16 and GOES-17 satellites, positioned at 75.2° W and 137.2° W, respectively, are geostationary satellites operated by the National Oceanic and Atmospheric Administration (NOAA). These satellites are equipped with the Space Environment In Situ Suite (SEISS) (Dichter et al., 2015; Kress et al., 2020) and a science magnetometer (MAG) (Loto'aniu et al., 2019; Rich et al., 2024). SEISS is capable of measuring electrons in the energy range of 30 eV to 4 MeV, protons in the range of 30 eV–500 MeV with an integral channel for energy >500 MeV, and heavy ions in the range of 10–200 MeV/nucleon. This study utilizes the Magnetospheric Particle Sensor-High (MPS-HI) from SEISS to measure electrons in the energy range of 50–4,000 keV. The MPS-HI comprises five electron telescopes with a 15° half-angle FOV each and coplanar centers spaced 35° apart. Boudouridis et al. (2020) presented a comprehensive explanation of how MPS-HI data processing is performed for 11 energy channels using a bow-tie inversion technique. The GOES-16 and -17 MAG are composed of two magnetometers, the inboard and outboard magnetometers, deployed on an 8.5-m-long boom. The MAG samples vector magnetic fields at a maximum rate of 10 Hz. The data used for the study are level-2 electron and magnetic field data averaged over 1-min intervals, obtained from the National Centers for Environmental Information of NOAA.

3. PSD Calculation in Invariant Coordinates

Electron PSD calculations for the GK2A, GOES-16, and GOES-17 satellites rely on a well-established relationship between PSD and differential flux (Schulz & Lanzerotti, 1974):

21699402, 2025, 4, Downloaded from https://agupubs.onlinelibrary.wiley.com/doi/10.1029/2024JA033161, Wiley Online Library on [02/10/2025]. See the Terms and Conditions (https://onlinelibrary.wiley.com/terms-and-conditions) on Wiley Online Library for rules of use; OA articles are governed by the applicable Creative Commons License

$$f = \frac{j}{p^2}, \tag{1}$$

where f is the electron PSD; j is the electron differential flux; and p^2 is the square of the relativistic momentum corresponding to the kinetic energy E. Their specific relationship is given as in Equation 2 below:

$$\left(E + m_0c^2\right)^2 = p^2c^2 + m_0^2c^4, \tag{2}$$

where m_0 is the electron rest mass and c is the speed of light.

According to Liouville's theorem, the PSD remains constant under the assumption of adiabatic invariants. For electrons trapped in the Earth's radiation belt, there are three adiabatic invariants related to the motions of gyration, bouncing, and drift (Roederer, 1970):

$$\begin{aligned} \mu &= \frac{p_\perp^2}{2m_oB} = \frac{\left(E^2 + 2m_oc^2E\right)\sin^2\alpha}{2m_oc^2B}, \\ K &= \int_{s_{m'}}^{s_m} \sqrt{B_m - B(s)}\,\mathrm{d}s, \\ L^* &= \frac{2\pi B_E R_E^2}{\int_\pi \boldsymbol{B}\cdot \mathrm{d}\mathbf{S}}, \end{aligned} \tag{3}$$

where μ is the first adiabatic invariant of the magnetic moment; $p_\perp^2$ is the square of the perpendicular relativistic momentum with respect to the local magnetic field strength B; α is the local pitch angle; K is the second adiabatic invariant; s_m and $s_{m'}$ are mirror points of electrons along the magnetic field lines; B_m is the strength of the magnetic field at mirror point; L^* is the third adiabatic invariant; B_E and R_E are the strength of the magnetic field and radius on the surface of the Earth, respectively; and finally, the denominator in the expression of L^* is the magnetic flux evaluated along the closed drift shell of electrons, where d$\mathbf{S}$ is a closed surface defined by the drift path of electrons and $\boldsymbol{B}$ represents magnetic field passing through the closed surface. A summary of the PSD calculation procedure used in this study is provided in Figure 2. The general procedure closely resembles that used in prior studies. Herein, we highlight a few key points:

- The calculation of the kinetic energy E corresponding to the selected first adiabatic invariant μ requires the measurement of local magnetic fields. Instead of relying on modeled magnetic fields, we used actual measurements from the geostationary satellites.
- To calculate K and L^*, the global magnetic field model TS05 (Tsyganenko & Sitnov, 2005) and the International Geomagnetic Reference Field in the International Radiation Belt Environment Modeling (IRBEM) library (Boscher et al., 2022) integrated into the SpacePy package (Niehof et al., 2022) were utilized. The solar wind parameters are one-minute averages of Operating Missions as a Node on the Internet (OMNI) parameters obtained from https://omniweb.gsfc.nasa.gov, whereas the magnetic field input parameters are obtained from https://iswa.ccmc.gsfc.nasa.gov/iswa_data_tree/composite/magnetosphere/Qin-Denton/1min/.
- PSDs corresponding to pairs of (μ, K), where the selected values of μ = 100, 150, 200, 250, 350, 500, 800, 1,000, 1,500, and 2,000 MeV/G and K = 0.02, 0.03, 0.04, 0.05, 0.07, and 0.1 $\mathrm{R_E}\sqrt{\mathrm{G}}$, were calculated. To minimize the occurrence of extrapolation in the energy spectrum fitting and PAD fitting processes, the maximum values of μ and K were limited. The maximum μ was set to 2,000 MeV/G, corresponding to approximately 1.6 MeV electrons. This upper limit was determined to essentially exclude the extrapolation in the energy spectrum fitting, taking into account that the detectors of the three satellites are capable of measuring energies exceeding 2 MeV. On the other hand, due to inherent limitations of geostationary satellites, pitch angle coverage is limited, which can result in significant data loss if the extrapolation of the PAD is completely prohibited. To address this issue, we ensured that the occurrence rate of extrapolation during PAD fitting remained below 10% when calculating PSD for specific μ and K combinations. After calculating the occurrence rate of extrapolation for various K values, we found that 0.1 $\mathrm{R_E}\sqrt{\mathrm{G}}$ was an appropriate threshold. The estimation of L^* for each of the PSDs follows, in conjunction with IRBEM in SpacePy. The PSD values were then grouped into bins along the L^* axis with a bin width of 0.1.

21699402, 2025, 4, Downloaded from https://agupubs.onlinelibrary.wiley.com/doi/10.1029/2024JA033161, Wiley Online Library on [02/10/2025]. See the Terms and Conditions (https://onlinelibrary.wiley.com/terms-and-conditions) on Wiley Online Library for rules of use; OA articles are governed by the applicable Creative Commons License

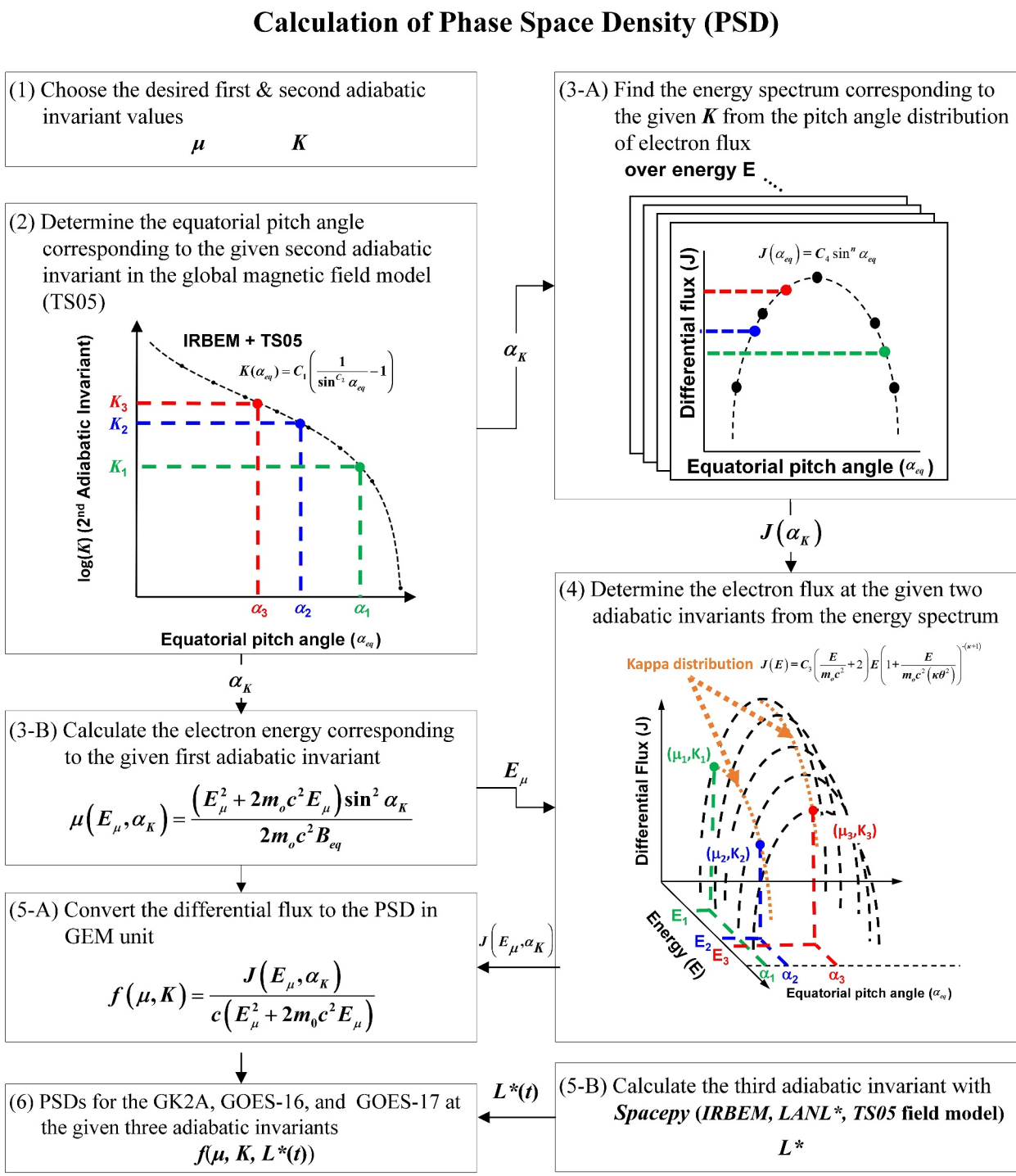

Figure 2. Procedure for calculating electron phase space densities (PSDs). A detailed explanation is provided in Section 3.

- To derive an empirical expression for K as a function of the equatorial pitch angle (α_{eq}), we calculated a finite number of K values corresponding to α_{eq} ranging from 10° to 90° at fixed intervals of 5°. The computed values of K were then employed to obtain a set of best-fit parameters, C_1 and C_2, under the assumption that K is a function of the following form:

21699402, 2025, 4, Downloaded from https://agupubs.onlinelibrary.wiley.com/doi/10.1029/2024JA033161, Wiley Online Library on [02/10/2025]. See the Terms and Conditions (https://onlinelibrary.wiley.com/terms-and-conditions) on Wiley Online Library for rules of use; OA articles are governed by the applicable Creative Commons License

$$K(\alpha_{eq}) = C_1\left(\frac{1}{\sin^{C_2}\alpha_{eq}} - 1\right). \tag{4}$$

- Using Equation 4, we can determine the values of α_{eq} for the selected K values. The local pitch angle α at the position of a geostationary satellite is related to α_{eq} through Equation 5, wherein B_{eq} is the estimated magnetic field strength at the magnetic equator from the field model, and B denotes the magnetic field strength measured by the geostationary satellite.

$$\frac{\sin^2\alpha}{B} = \frac{\sin^2\alpha_{eq}}{B_{eq}} \tag{5}$$

- The differential flux as a function of energy is represented by a kappa distribution (Livadiotis & McComas, 2013; Pierrard & Lazar, 2010; Whittaker et al., 2013; Xiao et al., 2008). There are various types of energy spectra existing in a radiation belt (Zhao, Johnston, et al., 2019), and the Kappa distribution used in the study does not perfectly describe all of them. In particular, sudden flux variations, such as the bump-on-tail reported by Zhao, Ni, et al. (2019), can significantly degrade the goodness of fit of the Kappa distribution. However, a prior study (Seol et al., 2023) demonstrated that the Kappa distribution generally outperforms double Maxwellian or power-law in the outer radiation belt. The Kappa distribution used in the study is given by Equation 6, which depicts this distribution in a relativistic form. Herein, the fitting constants C_3, θ, and κ are determined via the least squares fitting method with respect to measured fluxes at each energy bin.

$$J(E) = C_3\left(\frac{E}{m_o c^2} + 2\right)E\left(1 + \frac{E}{m_o c^2(\kappa\theta^2)}\right)^{-(\kappa+1)} \tag{6}$$

- The PAD is coarsely represented by the function expressed in Equation 7. It is important to note that owing to the limited sampling of pitch angles from the non-spinning geostationary satellites, each energy bin has only five or six differential fluxes available against the pitch angles for GOES or GK2A, respectively. As a result, a more sophisticated function for the PADs cannot be employed. The fitting parameters C_4 and n are determined using the least squares fitting method to account for the fluxes as a function of the pitch angle.

$$J(\alpha_{eq}) = C_4 \sin^n \alpha_{eq} \tag{7}$$

- Transformation between the invariant coordinates (μ, K) and measurable coordinates (E, α) is schematically illustrated in Figure 2.

4. Comparison of PSDs

In this section, we compare electron PSDs for geomagnetically quiet days from May to November 2019 based on measurements from the three geostationary satellites: GK2A, GOES-16, and GOES-17. This period coincides with that examined in an earlier study of GK2A observations (Seol et al., 2023) in which best-fit solutions to models of differential electron spectra were obtained over 39 energy bins to yield corrected instrument geometric factors for the PD instruments aboard the GK2A satellite. The data from GOES-16 and GOES-17 were calibrated against those from the earlier GOES series and Combined Release and Radiation Effects Satellite based on 10 differential electron channels and an integral electron channel above 2 MeV (Boudouridis et al., 2020). The electron PSDs were calculated from the electron fluxes measured by the satellites, in accordance with the method described in the previous section. Prior to this study, two distinct approaches have been used to compare the satellite measurements. The first method involves a direct comparison of flux measurements obtained from the satellites (Friedel et al., 2005; Szabó-Roberts et al., 2021; Wang et al., 2013; Zhang et al., 2018), whereas the second method involves a comparison of the PSDs derived from the flux in an adiabatic invariant coordinate system (Chen et al., 2007; Ni et al., 2009, 2011; Zhu et al., 2022). In the case of the direct comparison of fluxes, conjunction observations become essential, which necessitates the simultaneous measurement of the fluxes at the same location. On the other hand, the comparison of electron PSDs in the invariant coordinates of Liouville's theorem does not require conjunction

21699402, 2025, 4, Downloaded from https://agupubs.onlinelibrary.wiley.com/doi/10.1029/2024JA033161, Wiley Online Library on [02/10/2025]. See the Terms and Conditions (https://onlinelibrary.wiley.com/terms-and-conditions) on Wiley Online Library for rules of use; OA articles are governed by the applicable Creative Commons License

Table 1
List of Geomagnetically Quiet Days From May 2019 to November 2019 as Identified by the GeoForschungsZentrum German Research Center for Geosciences

Month	Days
May	5, 8, 19, 21, 25
June	6, 10, 11, 17, 23
July	19, 20, 26, 25
August	3, 9, 15, 19, 22
September	19, 20, 22, 23, 26
October	3, 13, 19, 22, 23
November	2, 3, 13

Note. For November 2019, only 3 days are included because of maintenance activities on the spacecraft after 14 November. The instrument was briefly turned off in November and fully recovered its operations in 2020.

observations. This flexibility allows us to compare the electron fluxes measured by the three geostationary satellites at different locations and times.

4.1. Data Selection

For the comparison of the electron PSDs, we restricted our data set to include only those obtained on geomagnetically quiet days because these days are more likely to fulfill the assumption of adiabatic invariance. First, we selected the quietest 5 days for each month, as identified by the GeoForschungsZentrum German Research Center for Geosciences (https://www.gfz-potsdam.de/en/kp-index/) (Matzka et al., 2021). The geomagnetically quiet days examined in this study are listed in Table 1. Herein, 6 July had been excluded because of the absence of data satisfying the conditions described in the following paragraph.

For each geomagnetically quiet day, the measurement samples for the subsequent PSD calculations were further narrowed down by imposing the following stringent set of conditions with respect to a number of commonly used geomagnetic indices (Joselyn, 1989):

$$K_P < 1 \text{ and } \mathrm{Dst} > -10 \text{ and } \mathrm{AE} < 50, \tag{8}$$

where Kp is the planetary K-index, Dst is the disturbance storm time index, and AE is the auroral electrojet index. After the conditions in Equation 8 were imposed, 15,255 samples of 1-min averaged OMNI parameters remained available for our analysis, corresponding to approximately 33% of the total duration of the 32 quiet days. It should be noted that among the three geomagnetic indices, the AE index was the most critical for reducing the number of samples, and that the conditions in Equation 8 were chosen to maintain the indices as stringent as possible while acquiring a sufficient amount of data for statistical significance.

We calculated the electron PSDs for specific times that fulfilled the conditions in Equation 8. As a first step toward this comparison, calculations were performed across a range of the first and second adiabatic invariants μ and K in accordance with the calculation procedure presented in Section 3. Overall, there were 60 combinations of μ and K with μ ranging from 100 to 2,000 MeV/G and K ranging from 0.02 to 0.1 $\mathrm{R_E}\sqrt{\mathrm{G}}$. The lower limit of μ was set to 100 MeV/G to account for the minimum energy channel of the electron flux measured by the GK2A satellite, whereas the upper limit was determined based on the maximum energy observed in the electron fluxes measured by the three satellites. For the second adiabatic invariant, the selected range of K ensured the collection of a sufficient amount of data. Outside this selected range, the amount of data sharply decreases; electrons with large pitch angles (small K) may not reach the satellites off the magnetic equator owing to near-equatorial mirroring, whereas electrons with small pitch angles (large K) remain unobserved because of their inclusion within the loss cone. The third adiabatic invariant L^* was calculated at one-minute intervals based on the pitch angle corresponding to a selected parameter (K) at the satellite's position. Determining the pitch angle associated with the chosen K involved interpolating K values using the measured pitch angles from each FOV boresight. The values of L^* for the pitch angle matching the chosen K were initially computed using either IRBEM (Boscher et al., 2022) or Los Alamos National Laboratory L^* (LANL*) (Koller et al., 2009) in conjunction with the global magnetic field model TS05 (Tsyganenko & Sitnov, 2005). The IRBEM library provides an accurate estimation of L^* by numerically tracing magnetic field lines at the expense of computer CPU time. In this study, the magnitudes of L^* were computed using the LANL* model after the expected CPU time required to process approximately 7 months of data was considered. The resulting L^* values were binned with a bin size of 0.1, selected somewhat arbitrarily but generally aligned with the validation findings on the LANL* model (Koller & Zaharia, 2011). For geomagnetically quiet days that satisfy the conditions in Equation 8, this process yielded L^* values within the range of approximately 5.8–7.0. For example, the bottom panel of Figure 3 shows that the L^* variations for the 7th and 8th of May in 2019 fall within the previously mentioned L^* range. A summary of the selected values for parameters μ, K, and L^* is provided in Table 2.

For the subsequent step in comparing electron PSDs, we took advantage of the occasional alignment of the third adiabatic invariant at certain times of the day, which was possible because of the distinct magnetic latitudes of the

21699402, 2025, 4, Downloaded from https://agupubs.onlinelibrary.wiley.com/doi/10.1029/2024JA033161, Wiley Online Library on [02/10/2025]. See the Terms and Conditions (https://onlinelibrary.wiley.com/terms-and-conditions) on Wiley Online Library for rules of use; OA articles are governed by the applicable Creative Commons License

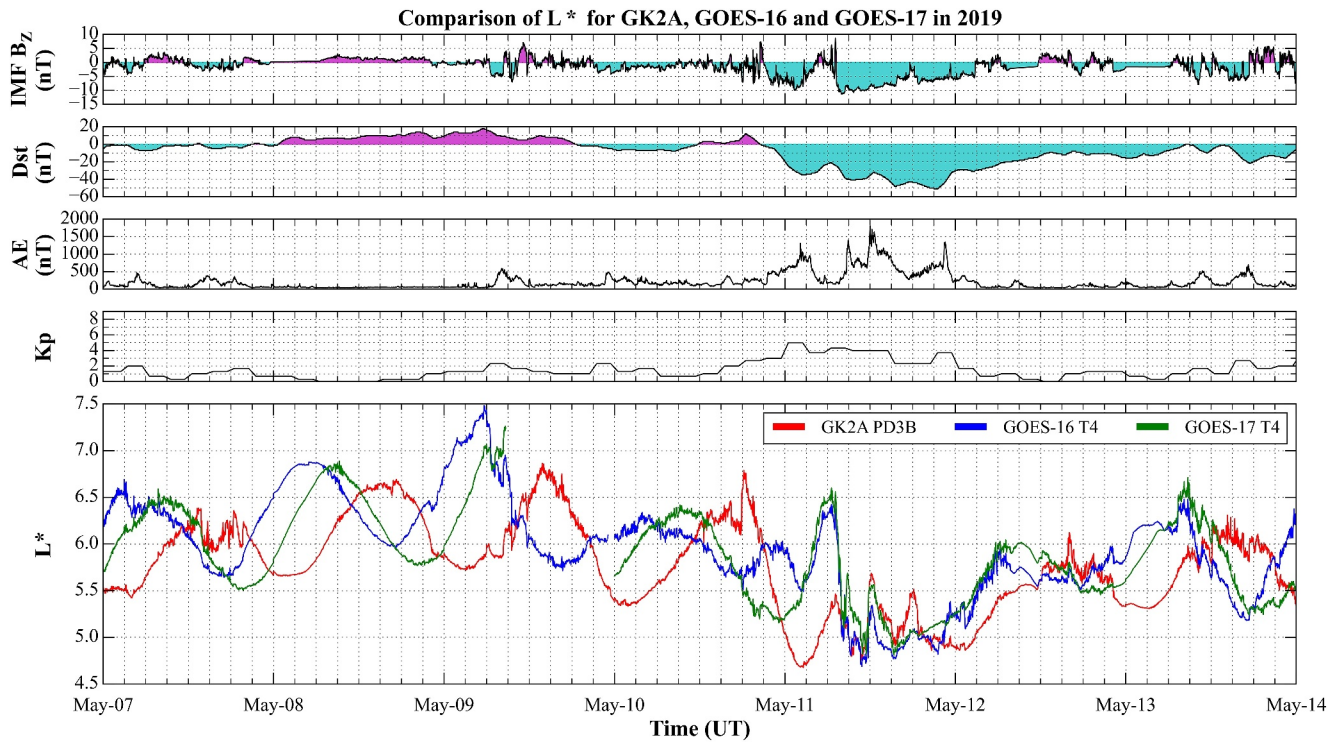

Figure 3. Comparison of third adiabatic invariant (L^*) values for 7–14 May 2019 based on (from top to bottom) interplanetary magnetic field (IMF) in north–south direction (B_Z), disturbance storm time (Dst) index, auroral electrojet (AE) index, planetary K-index (K_P), and L^*. Cyan and magenta areas in IMF B_Z and Dst plots indicate negative and positive values, respectively. Third adiabatic invariants for each satellite are shown in bottom panel. Red, blue, and green lines denote PD3B of GK2A, T4 of GOES-16, and T4 of GOES-17, respectively.

three geostationary satellites. An example of an actual L^* conjunction is illustrated in Figure 3. Herein, the L^* values were computed for the PD3B detector of GK2A and the T4 detectors of GOES-16 and GOES-17 from 7 May to 14 May 2019. These detectors had FOVs close to the equatorial plane. Moreover, a moderately sized geomagnetic storm ($K_P < 5$) was observed during this time with a sudden commencement at approximately 1757 UT on 10 May. The data in the figure demonstrate that L^* often exhibits periodic diurnal trends, with smaller L^* magnitudes near local noon and greater magnitudes near local midnight, preceding sudden commencement. It is noteworthy that, as can be clearly seen in Table 1, only one date from this period, that is, 8 May, was chosen for electron PSD comparison in accordance with the criteria presented in Section 4.1 for the quietest five days of each month. The computed L^* values, binned in sizes of 0.1, were considered identical if they fell within the same bin. For the final step of the PSD comparison, we imposed a constraint on our analysis that the observation time of a pair of satellites must coincide, with a maximum allowable time difference of one minute. In other words, we regarded the electron PSD as a function of μ, K, L^*, and time, aligning these parameters for our comparison. This alignment of the adiabatic invariants μ, K, and L^* in conjunction with time t was essential because it was evident that the electron PSDs could not be adiabatically mapped if they were temporally distant under the varying conditions of solar wind and geomagnetic activity. The validity of the adiabatic assumption appears to hold intermittently, at best, over only a limited duration during geomagnetically quiet times.

Table 2
Selected Values of First (μ), Second (K) and Third (L^*) Adiabatic Invariants for Estimating Phase Space Densities in Geomagnetically Quiet Periods

Adiabatic invariant	Values
μ (MeV/G)	100, 150, 200, 250, 350, 500, 800, 1,000, 1,500, 2,000
K ($R_E\sqrt{G}$)	0.02, 0.03, 0.04, 0.05, 0.07, 0.1
L^*	5.8–7.0 (bin size 0.1)

Note. For μ, the lower and upper limits are determined by accounting for the energy ranges of the three satellites. For K, the selected range of values considers both electrons confined to the geomagnetic equator (small K) and those capable of escaping through the loss cone (larger K). For L^*, the values correspond to the center of each bin, each having a width of 0.1.

Figure 4 shows histograms of the L^* values for the three pairings of the geostationary satellites. The top panels show distributions of the electron PSDs in L^* space for all values of μ and K in Table 2. Each PSD in the top panels shares a specific set of adiabatic invariants μ and K at time t. The figure shows that the numbers of PSDs were 457,480 for the GK2A and GOES-16 pair (GK2–G16), 525,890 for the GK2A and GOES-17 pair (GK2–G17), and

21699402, 2025, 4, Downloaded from https://agupubs.onlinelibrary.wiley.com/doi/10.1029/2024JA033161, Wiley Online Library on [02/10/2025]. See the Terms and Conditions (https://onlinelibrary.wiley.com/terms-and-conditions) on Wiley Online Library for rules of use; OA articles are governed by the applicable Creative Commons License

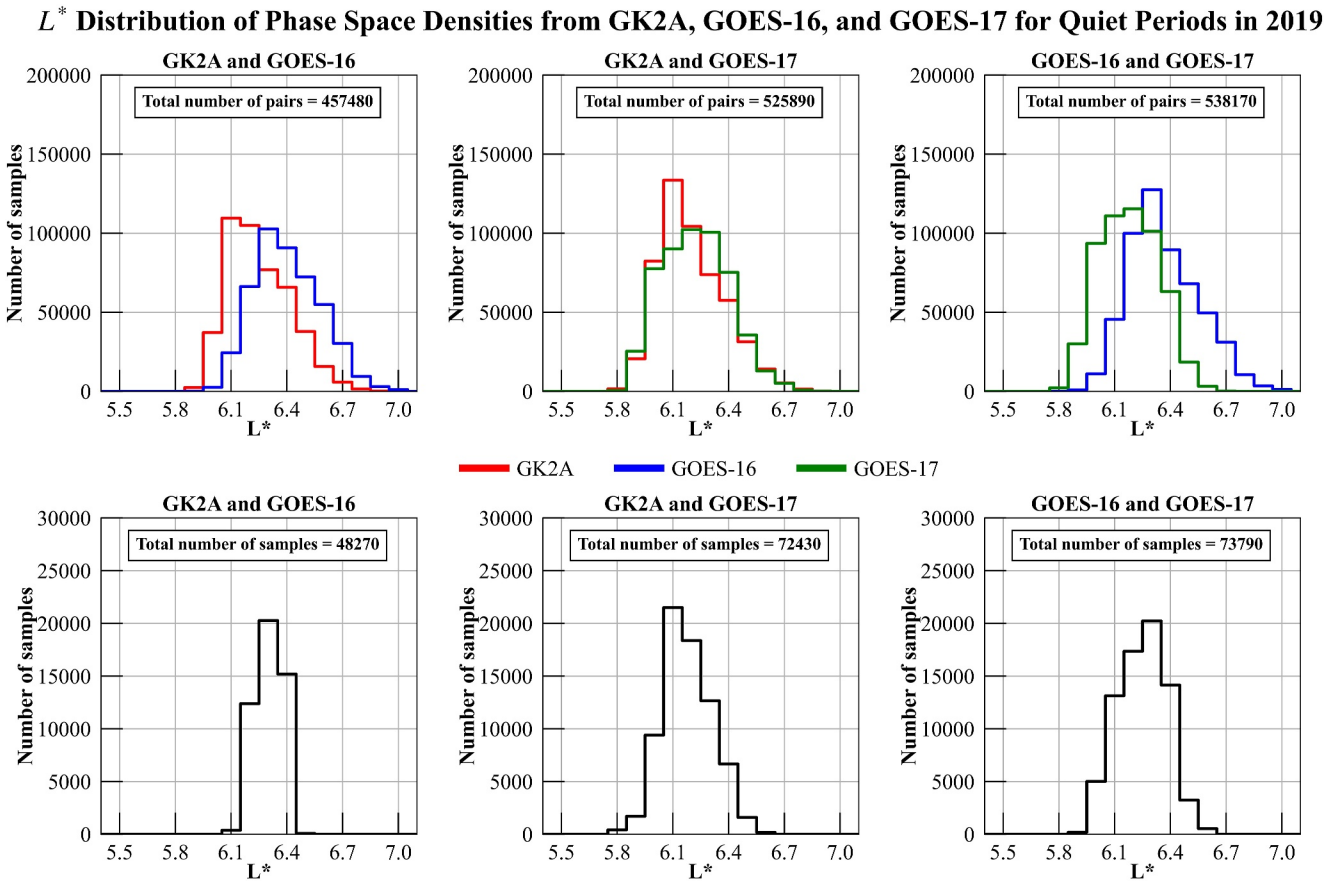

Figure 4. Histograms of L^* values before and after L^* conjunction for geomagnetically quiet periods. Upper panels present L^* distributions of electron PSDs obtained from the satellites for the same μ, K, and time in a geomagnetically quiet phase. Red, blue, and green indicate GK2A PSDs, GOES-16 PSDs, and GOES-17 PSDs, respectively. Lower panels summarize results of comparisons of electron PSDs at conjunction for the three adiabatic invariants and time. Number of conjunction observations is also indicated in each lower panel. Lower histograms show that conjunction of satellites in L^* likely occurred at approximately $L^* \sim 6.0$–6.5.

538,170, for the GOES-16 and GOES-17 pair (G16–G17). An examination of the top panels finds that, on average, the L^* values follow the order GOES-16 > GK2A > GOES-17, corresponding to the relative magnitudes of the magnetic latitudes. On the other hand, the histograms in the bottom panels present distributions derived from those in the upper panels, with a constraint that the L^* bin values must be the same at time t. This constraint resulted in reduced numbers for the PSD samples, totaling 48,270 for GK2–G16, 72,430 for GK2–G17, and 73,790 for G16–G17. Note that the histograms show that the conjunction of satellites in L^* likely occurred at approximately $L^* \sim 6.0$–6.5. Later in the study, as described in Section 4.2 the data sets from the lower panels will be used to compare the PSDs among the satellites.

4.2. PSD Comparison Results

In Figure 5, the PSDs are compared using scatter plots for the data sets outlined in Section 4.1. These data sets were selected based on criteria for the geomagnetic conditions, defined in Equation 8, followed by alignment of the three adiabatic invariants and time for the three geostationary satellites. The scatter plots illustrate PSD comparisons among the satellite pairings, that is, GK2–G16, corresponding to 48,270 pairs of PSD values; GK2–G17, corresponding to 72,430; and G16–G17, corresponding to 73,790. From top to bottom, each row represents identical data sets in terms of the three adiabatic invariants μ, K, and L^*. The color-coded legends positioned at the bottom of the upper row denote the magnitudes of the first adiabatic invariant. Additionally, dashed diagonal red lines serve as guides for assessing the agreement of PSDs between the satellite pairs, whereas accompanying gray dashed lines positioned above and below the red lines indicate PSD ratios of 2, 5, and 10 and their inverses, respectively. The R^2 is the coefficient of determination that indicates how close the data are to the

21699402, 2025, 4, Downloaded from https://agupubs.onlinelibrary.wiley.com/doi/10.1029/2024JA033161, Wiley Online Library on [02/10/2025]. See the Terms and Conditions (https://onlinelibrary.wiley.com/terms-and-conditions) on Wiley Online Library for rules of use; OA articles are governed by the applicable Creative Commons License

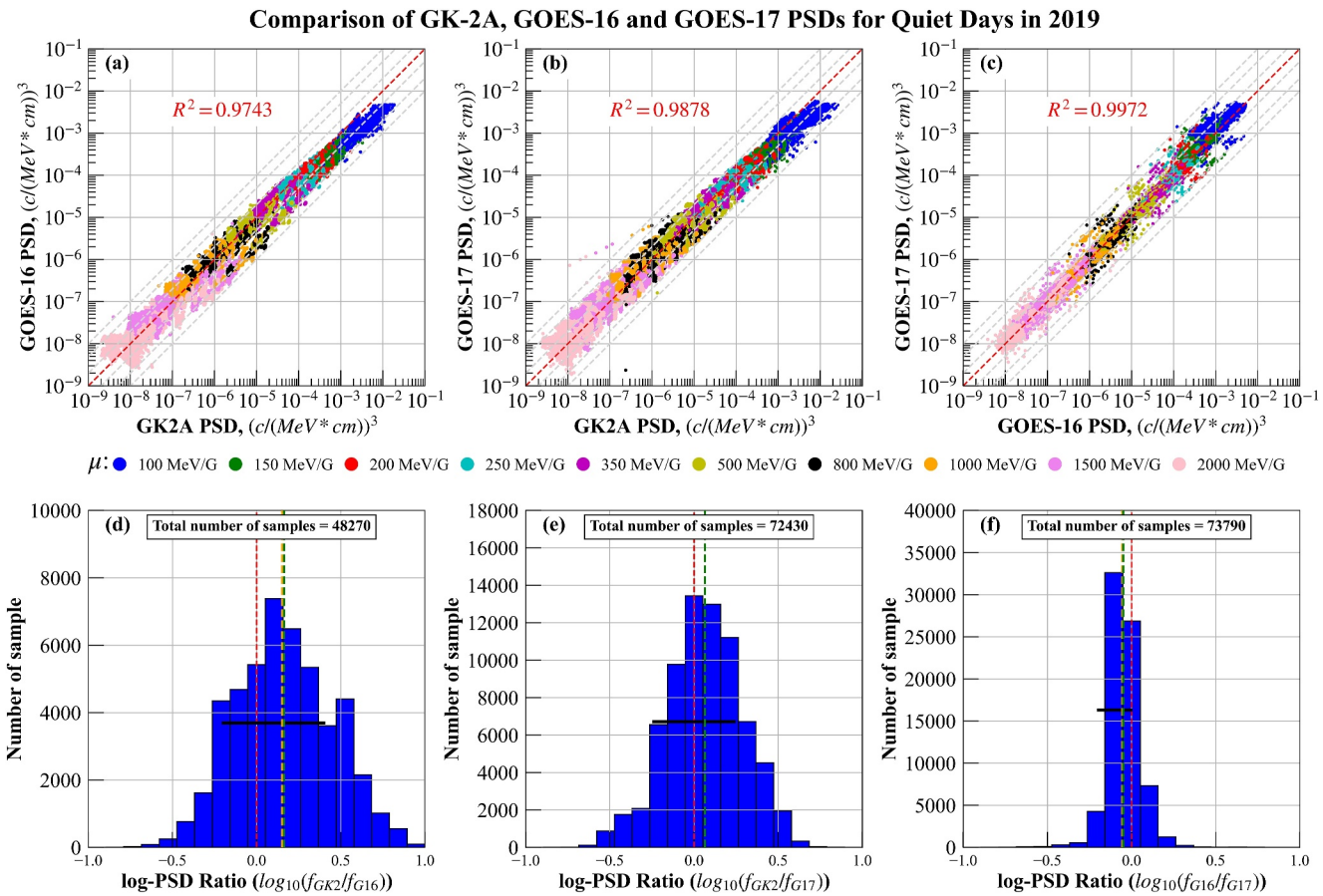

Figure 5. Scatter plots of electron PSDs for geomagnetically quiet periods before cross-satellite calibration: (a) GOES-16 versus GK2A, (b) GOES-17 versus GK2A, (c) GOES-16 versus GOES-17; in each scatter plot, marker colors represent first adiabatic invariant values. Histograms of PSD ratios: (d) $\log_{10}\left(f_{GK2}/f_{G16}\right)$, (e) $\log_{10}\left(f_{GK2}/f_{G17}\right)$, (f) $\log_{10}\left(f_{G16}/f_{G17}\right)$. Red dashed lines indicate perfect calibration. Gray dashed lines in (a)–(c) denote PSD ratios of 2, 5, 10, and their inverses, respectively. Solid black line, dashed green line, and dashed orange line indicate full width at half maximum (FWHM), mean, and median of histogram, respectively. Before calibration, slight offsets occur in all satellite pairs, with the smallest difference between GOES-16 and GOES-17, and the largest between GK2A and GOES-16. The coefficient of determination R^2 for the identity line and data is 0.9743 for GK2–G16, 0.9878 for GK2–G17, and 0.9972 for G16–G17.

identity line. The data in the figure show that, for geomagnetically quiet days, there is generally good agreement in the electron PSDs, depending on the energy of the electrons. It is worth mentioning that this agreement between GOES-16 and GOES-17 is somewhat anticipated, given their identical instrument designs and data processing algorithms, and their closer proximity compared to the angular distance between GK2A and the GOES satellites. In Figure 5a, we observe a trend that the GK2A PSDs are consistently larger than those from GOES-16, particularly for smaller first adiabatic moments such as $\mu = 100$ MeV/G (represented by filled circles in blue). In these cases, the PSDs obtained using GK2A can be approximately two to four times greater than those obtained using GOES-16, suggesting the possibility of systematic differences between the satellites.

The histograms of the PSDs of the scatter plots discussed herein are presented in the lower panels of Figure 5. Each histogram panel illustrates the distribution of PSD ratios between specific paired satellites. From left to right, the histograms correspond to the PSD ratios for GK2–G16, GK2–G17, and G16–G17. Each histogram bins the base-10 logarithm of the PSD ratio between the satellites of a specific pair along the horizontal axis. The bin width is 0.1, signifying that for each increment in the bin, the PSD ratio increases by a factor of 1.259. The vertical axis represents the number of accumulated ratios for each bin. Red, orange, and green dashed lines indicate perfect calibration, median value of the log-PSD ratios, and mean value of the log-PSD ratio, respectively. These histograms validate the qualitative observations regarding Figure 5, confirming that, on average, the PSDs measured using GK2A exceed those obtained using GOES-16 and GOES-17. The results of the histograms also support the finding that GOES-16 and GOES-17 have a notably better agreement between their PSDs, as

21699402, 2025, 4, Downloaded from https://agupubs.onlinelibrary.wiley.com/doi/10.1029/2024JA033161, Wiley Online Library on [02/10/2025]. See the Terms and Conditions (https://onlinelibrary.wiley.com/terms-and-conditions) on Wiley Online Library for rules of use; OA articles are governed by the applicable Creative Commons License

Table 3
Statistics Related to Histogram Shape Before and After Cross-Satellite Calibration: Mean, Median, and Bin Width

	Log_{10} of PSD ratio					
	Before calibration			After calibration		
Satellite pair	Mean	Median	FWHM	Mean	Median	FWHM
GK2–G16	0.1631	0.1516	0.6149	0.0578	0.0393	0.6036
GK2–G17	0.0651	0.0648	0.4950	0.0048	0.0025	0.4829
G16–G17	−0.0483	−0.0552	0.2116	−0.0047	−0.0102	0.1705

indicated by a narrower distribution centered around a ratio of 1 in the rightmost panel compared with the broader distributions shown in the leftmost and middle panels.

4.3. Intersatellite Calibrations

In the previous part of the study, we conducted a comparative analysis of the electron PSDs computed from electron fluxes measured by the three geostationary satellites. Overall, the PSD estimations yielded consistent outcomes during periods of geomagnetically quiet conditions as defined by Equation 8. For a more detailed assessment, we analyzed the shapes of the histograms. Specifically, we investigated the full width at half maximum (FWHM) and skewness of the histograms. The statistics related to the shape of the histogram before and after calibration are summarized in Table 3.

The FWHMs of the histograms are illustrated as black horizontal lines in the lower panels of Figure 5. As shown in Table 3, the FWHM for the GK2A and GOES satellites typically fell within a range of approximately 0.49–0.62 (corresponding to approximately three to four in PSD ratio). The FWHM was further improved to within a factor of approximately 0.21 (corresponding to approximately 1.6 in PSD ratio) when the PSDs from the two GOES satellites were compared.

The skewness of the histogram for each satellite pair was assessed using the mean and median values of the log-PSD ratios. A greater skewness would imply more substantial discrepancies between the instrument responses. As shown in Table 3, for the GK2–G17 pair before calibration, the mean and median values of the log-PSD ratios were 0.0651 and 0.0648, respectively, whereas for the GK2–G16 pair, the values before calibration were 0.1631 and 0.1516, respectively. For the G16–G17 pair, the values before calibration further decreased to −0.0483 and −0.0552, respectively. The gaps between the mean and median for the GK2–G16, GK2–G17, and G16–G17 pairs were 0.0003, 0.0115, and 0.0069, respectively. These values correspond to 1.000, 1.026, and 1.016, respectively, in PSD ratio, which are quite close to one. Based on these results, we concluded that all of the histograms were not highly skewed and that the instrument responses were quite similar to each other. However, from the deviations of the mean (green) and median (orange) from the perfect calibration line (red), it is evident that offsets exist between the satellite pairs. To ensure more precise comparisons among the geostationary satellites, it is necessary to assimilate the PSD estimations by decreasing the offsets.

In this study, we adjusted the GK2A PSDs and GOES-16 PSDs to align with those obtained from GOES-17 as follows: First, to eliminate unnecessary bias from the outliers of the data set during the assimilation process, the PSD ratio was set to an arbitrary range of 10^{-5} to 10^{5} to screen the data sets for each of the satellite pairs. Outliers were generated by poor energy or pitch angle fitting during PSD calculation. As a result of this screening, among the PSD pairs for the geomagnetically quiet periods, only three PSD pairs were removed from the 525,890 pairs for the GK2–G17 pair and the 538,170 pairs for the G16–G17 pair. For the conjunction observations, only one PSD pair was removed from the 72,430 pairs for the GK2–G17 pair, whereas there was no change in the number of pairs for the G16–G17 pair.

Next, we used the base-10 logarithm of the PSDs to linearly fit the GK2A PSDs and GOES-16 PSDs against the GOES-17 PSDs. In the fitting of the PSDs, uncertainties in the PSDs obtained using the three satellites were considered by employing the orthogonal distance regression (ODR) method (Boggs & Rogers, 1990). The goodness-of-fit was assessed by presenting coefficient of determination, R^2, for the data relative to the identity line before and after calibration. The uncertainties in the GK2A electron fluxes were derived from the measured electron fluxes using conventional uncertainty propagation equations (see Appendix A: Uncertainty in Electron PSD). These uncertainties of differential fluxes include contributions from the Poisson statistics, along with those from the finite energy bin widths. Similarly, the uncertainties in the GOES PSDs were derived from the level-2 electron fluxes distributed by the NOAA National Centers for Environmental Information (https://ngdc.noaa.gov/).

The ODR method yielded a multiplication factor of $10^{a+b\,\log_{10} f}$, which was subsequently applied to modify the GK2A and GOES-16 PSDs for assimilation; the constants a and b were obtained from the fitting, whereas f is used to represent the PSD values of the GK2A and GOES-16 satellites. The multiplication factors derived from the

21699402, 2025, 4, Downloaded from https://agupubs.onlinelibrary.wiley.com/doi/10.1029/2024JA033161, Wiley Online Library on [02/10/2025]. See the Terms and Conditions (https://onlinelibrary.wiley.com/terms-and-conditions) on Wiley Online Library for rules of use; OA articles are governed by the applicable Creative Commons License

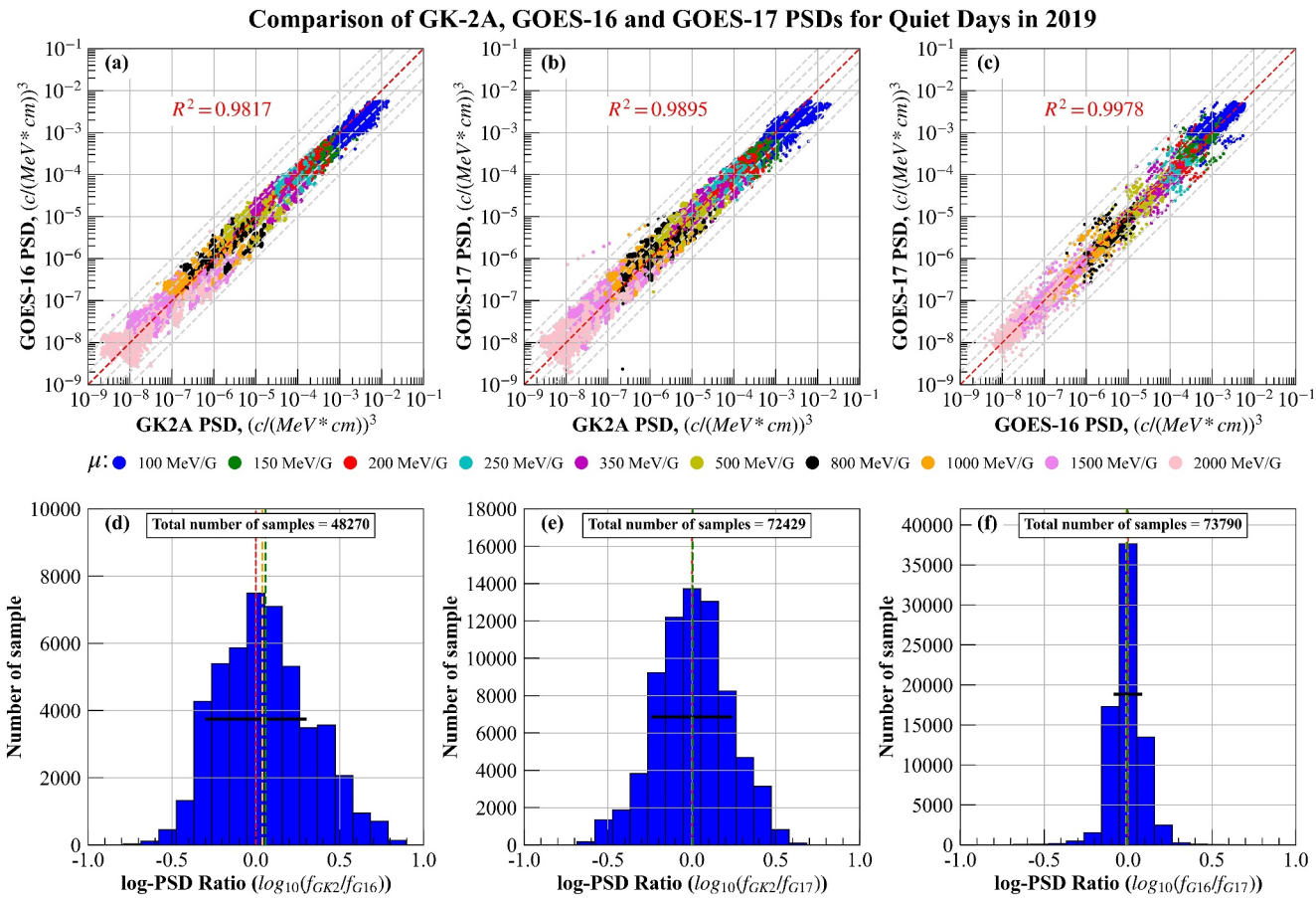

Figure 6. Scatter plots of electron PSDs for geomagnetically quiet periods after cross-satellite calibration: (a) GK2–G16, (b) GK2–G17, (c) G16–G17; in each scatter plot, marker colors represent first adiabatic invariant values. Histograms of PSD ratios: (d) $\log_{10}(f_{GK2}/f_{G16})$, (e) $\log_{10}(f_{GK2}/f_{G17})$, (f) $\log_{10}(f_{G16}/f_{G17})$. Red dashed lines indicate perfect calibration. Gray dashed lines in (a)–(c) denote PSD ratios of 2, 5, 10, and their inverses, respectively. Solid black line, dashed green line, and dashed orange line indicate FWHM, mean, and median of histogram, respectively. After calibration, no offsets are observed for GK2–G17 and G16–G17. Agreement between GK2 and G16 is improved, with mean of log-PSD ratio decreasing from 0.1631 to 0.0578, and median decreasing from 0.1516 to 0.0393, approaching closer to zero. The coefficient of determination R^2 is 0. 9817 for GK2–G16, 0.9895 for GK2–G17, and 0.9978 for G16–G17.

fitting are $10^{-(0.1474 \pm 0.0026) + (0.9824 \pm 0.0005)\log_{10} f_{gk2}}$ for GK2A and $10^{(0.0971 \pm 0.0009) + (1.0111 \pm 0.0002)\log_{10} f_{g16}}$ for GOES-16, respectively. For the GK2A PSD correction, larger reductions in the PSD magnitudes were noted for larger PSDs. For the G16 PSD, the correction factor increased for larger PSDs. With these multiplication factors, the electron PSDs of the GK2A and GOES-16 satellites were adjusted. In Figure 6, scatter plots of the satellite PSD pairs and a histogram of the PSD ratios are provided in the same format as that used in Figure 5. Upon examining the upper panels of Figures 5 and 6, it can be observed that R^2 for each satellite pair increased slightly, for the GK2–G16, GK2–G17, and G16–G17 pairs, from 0.9743, 0.9878, and 0.9972 to 0.9817, 0.9895, and 0.9978, respectively. Furthermore, as shown in the bottom row, the offsets for the GK2–G17 and G16–G17 pairs were eliminated, and the agreement between GOES-16 and GK2A showed a slight improvement. The specific statistical values after calibration are also presented in Table 3. We will utilize these corrected GK2A and GOES-16 PSDs for comparison with the GOES PSDs in the next part of the study.

5. Discussion

The conjunction of the geostationary satellites in (μ, K, L^*) coordinates allows for PSDs obtained in geomagnetically quiet periods to be compared between pairs of satellites. Subsequent intersatellite calibration enables the assessment of PSD gradients. With this comparison and intersatellite calibrations, satellite pairing provides unique opportunities to estimate the radial gradient of a PSD via the collection of PSD samples along the third adiabatic invariant L^*. This estimation is made possible by the three geostationary satellites traversing different L^*

21699402, 2025, 4, Downloaded from https://agupubs.onlinelibrary.wiley.com/doi/10.1029/2024JA033161, Wiley Online Library on [02/10/2025]. See the Terms and Conditions (https://onlinelibrary.wiley.com/terms-and-conditions) on Wiley Online Library for rules of use; OA articles are governed by the applicable Creative Commons License

values owing to different magnetic latitudes for most of the observation times, while occasionally staying close in terms of L^*, as exemplified in Figure 3. This gradient is closely linked to the processes of electron injection, transport, acceleration, and loss within the radiation belt. Past studies have extensively examined the signs of PSD slopes near geostationary orbits, which serve as crucial indicators for distinguishing between internal and external sources of acceleration. A number of competing observations and analyses have been reported.

Selesnick and Blake (2000) identified peaks in PSD at L^* between 4 and 6 for μ = 200 and 800 MeV/G and $K = 1.0\ \mathrm{R_E}\sqrt{\mathrm{G}}$. Taylor et al. (2004) noted a steep outward PSD gradient near the geosynchronous orbit, followed by a moderately flat to rising outward gradient into the plasma sheet near 18 R_E. Green and Kivelson (2004) calculated PSD as a function of μ, K, and L^* using Polar data. They also found peaks in the relativistic PSD profiles, considering uncertainties in the results due to model error when calculating K for high-latitude Polar observations. Onsager et al. (2004) found that the radial gradient of PSD was positive at μ = 6 GeV/G in geosynchronous orbit during geomagnetically quiet periods. Chen et al. (2005) compared multi-satellite measurements to determine the global PSD gradient near L^* = 6–7, addressing the sensitivity of their method to the choice of the magnetic field model and the fidelity of instrument intercalibration. They found positive radial slopes for low-energy density distributions during magnetically quiet periods, contrasting with the negative slopes at high energies. Chen et al. (2007) provided observational evidence for local acceleration as a source of relativistic electrons, presenting peaked distributions in off-equatorial PSD distributions in (μ, K, L^*) coordinates. Turner and Li (2008) found that the PSD distributions of near-equatorial electrons were μ-dependent beyond geosynchronous orbit prior to sudden solar wind pressure enhancements. The signs of the PSD gradients were often positive for low-energy (<~200 MeV/G) electrons but negative for those at higher energy, indicating different source regions for the two populations. H.-J. Kim et al. (2010) conducted a similar study with consistent results for off-equatorial electrons. Turner et al. (2012) found an energy-dependent profile for equatorial electron PSDs in the outer belt, suggesting different source regions for relativistic and non-relativistic populations. Schiller et al. (2014) examined PSD profiles from the Van Allen Probe, revealing a positive outward radial gradient within the range of $4 < L < 5.5$, while observations from the THEMIS satellites showed a PSD peak beyond the Van Allen Probes' apogee. The researchers thus suggested that acceleration of the charged particles occurred near $L^* \sim 5.5$, followed by rapid radial inward transportation. Liu et al. (2020) found that the radial distributions of PSD are μ-dependent, K-dependent, and azimuthally asymmetric from the Magnetospheric Multiscale Mission observations. Recently, Olifer et al. (2021) analyzed the in-bound pass of Van Allen Probe A to suggest that an apparent local PSD peak, although not real, may appear owing to rapid radial diffusion, based on a conjunction analysis on the two Van Allen Probes.

Our analysis addressed the important question on the PSD radial gradient near geostationary orbits. Note that our observations will not be affected by time aliasing, given that the measurements from the three geostationary satellites occurred simultaneously. Furthermore, our analysis enabled us to explore the frequency of positive or negative PSD gradients near geostationary orbits, benefiting from data sets spanning a longer duration from May to November 2019, rather than being constrained by an isolated single or a limited number of observations.

Figure 7 presents three 2D histograms corresponding to the three pairings of the geostationary satellites. In each panel of the upper row, the horizontal axis denotes the difference between the paired geostationary satellites, whereas the vertical axis denotes the logarithm of the PSD ratio, defined as $\log_{10}\left(f_{sat1}/f_{sat2}\right)$. When constructing the 2D histograms, we assigned a bin width of 0.1 to the horizontal axis, taking into account the uncertainties in L^* (refer to Appendix B: Uncertainty in L^*). To clearly show the distribution of the PSD ratios, the bin width of the vertical axis was set to 0.05. These histograms were generated using a data set obtained during geomagnetically quiet periods, identical to that described in Section 4.

The occurrences in each bin of the 2D histogram are color coded in accordance with the color bar displayed on the right-hand side of each plot. In each histogram, positive gradients of the PSDs occur in the first and third quadrants of the plane, whereas negative gradients occur in the second and fourth quadrants. The results of the 2D histograms are further summarized in the bottom row of the figure. Each plot in this row illustrates the ratio of positive to negative slopes, derived from the differences between the L^* values and the ratio of PSDs for the individual satellite pairs in the upper row. The results of the analysis suggest that, during geomagnetically quiet periods, there is a notable tendency for a greater number of observations to exhibit positive PSD gradients against radial distances represented by L^* for geostationary orbits.

21699402, 2025, 4, Downloaded from https://agupubs.onlinelibrary.wiley.com/doi/10.1029/2024JA033161, Wiley Online Library on [02/10/2025]. See the Terms and Conditions (https://onlinelibrary.wiley.com/terms-and-conditions) on Wiley Online Library for rules of use; OA articles are governed by the applicable Creative Commons License

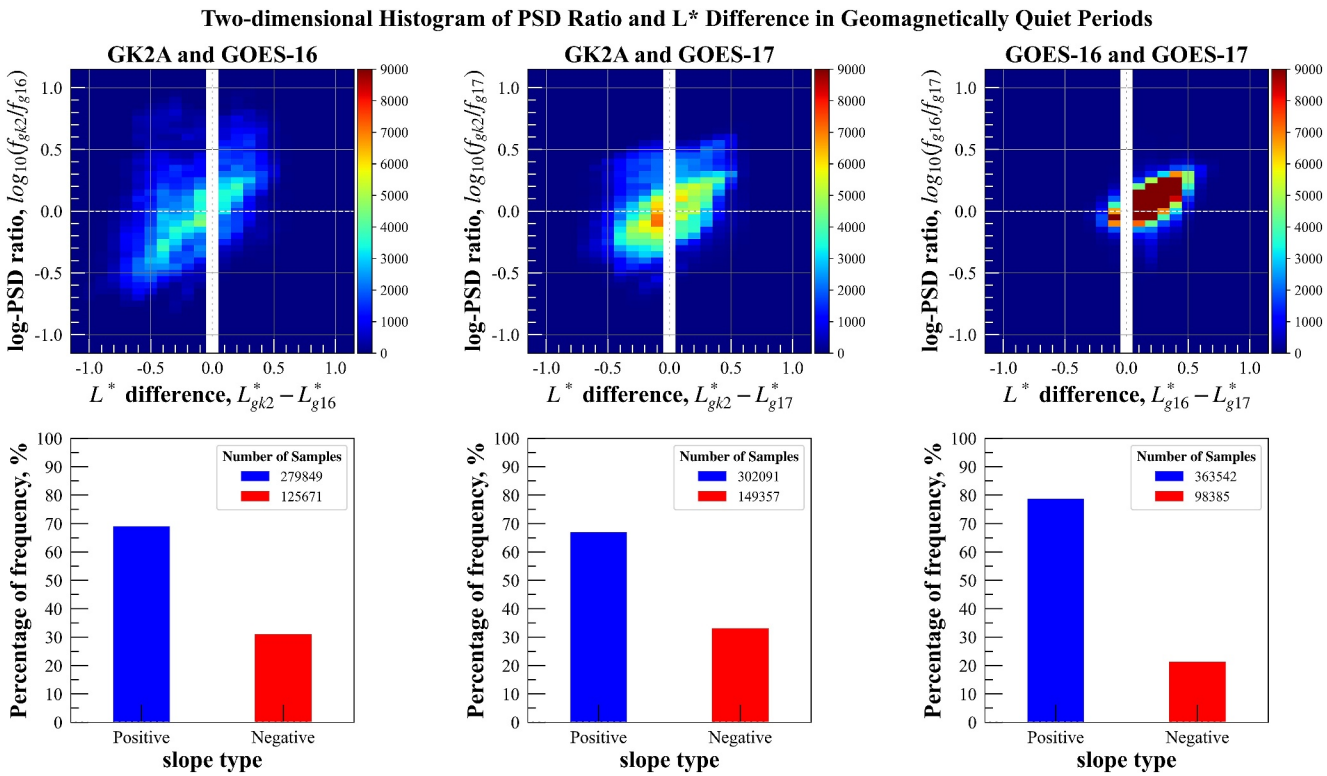

Figure 7. Two-dimensional histograms of log-PSD ratio and L^* difference in geomagnetically quiet periods (from left to right): GK2A and GOES-16, GK2A and GOES-17, and GOES-16 and GOES-17. Each upper-row grid of panels represents a PSD gradient. First and third quadrants indicate positive gradients; second and fourth quadrants indicate negative gradients. Frequencies are color coded in accordance with right-side color bar of each upper-row panel. L^* difference bins in 0.1 increments account for errors in L^*, whereas log-PSD ratio is represented in logarithmic form of f_1/f_2 to show symmetry around zero. Lower-row panels present frequency percentages of positive and negative slopes for corresponding upper-row panels. Blue bars represent percentages of samples with positive slopes, whereas red bars represent those with negative slopes. The numbers of samples for each category are indicated. Predominance of positive gradients is observed for all satellite pairs.

A more detailed examination of the PSD gradients in terms of the first and second adiabatic invariants is shown in Figure 8, with which we can examine the PSD gradient distribution more precisely according to the combinations of μ and K. The panels in the upper row show the PSD gradients at smaller K values of 0.02 and 0.03 $R_E\sqrt{G}$ to examine electrons near the magnetic equator. The panels in the lower row show the PSD gradients at larger K values of 0.7 and 0.1 $R_E\sqrt{G}$ to investigate electrons moving closer to the geomagnetic poles. The vertical axis of each panel indicates whether the gradient is positive or negative. To illustrate the tendencies of the PSD gradients in a symmetrical manner, we define the log-PSD gradient as $\log_{10}\left(f_{sat1}/f_{sat2}\right)/\Delta L^*$. In this representation, zero indicates no gradient in the PSD distribution, whereas positive and negative values indicate that the PSD increases outward and inward, respectively. The horizontal axis represents the values of the first adiabatic invariants. The solid black boxes represent the interquartile range (IQR). The lower ($Q1$) and upper ($Q3$) bases of the boxes represent the medians of the lower and upper halves of the log-PSD gradients, respectively. The solid orange and green lines within the boxes indicate the medians and means of the log-PSD gradients, respectively. The whiskers extending from the boxes denote the range from $Q1 - 1.5$IQR to $Q3 + 1.5$IQR, indicating the upper and lower limits of the log-PSD gradients. The data points beyond the whiskers are marked with a "+" symbol, indicating that they can be considered outliers. As reference, ΔL^* is binned in 0.1-unit intervals, and ΔL^* values greater than 0.1 are used to calculate the log-PSD gradient.

The potential existence of a radial gradient depending on the first adiabatic invariant, μ, has been extensively examined in previous studies (Boyd et al., 2014; X. Li et al., 1999; Sarris et al., 2021; Turner et al., 2012) and is similarly observed in our analysis. This trend is particularly evident in the GK2–G16 and G16–G17 data set pairs, as shown in the left and right of Figure 8. However, for larger K ($K = 0.07, 0.1\ R_E\sqrt{G}$) this trend is not apparent in the GK2–G17 pair (bottom middle panel). It is hypothesized that this deviation of GK2–G17 pair is partly related

21699402, 2025, 4, Downloaded from https://agupubs.onlinelibrary.wiley.com/doi/10.1029/2024JA033161, Wiley Online Library on [02/10/2025]. See the Terms and Conditions (https://onlinelibrary.wiley.com/terms-and-conditions) on Wiley Online Library for rules of use; OA articles are governed by the applicable Creative Commons License

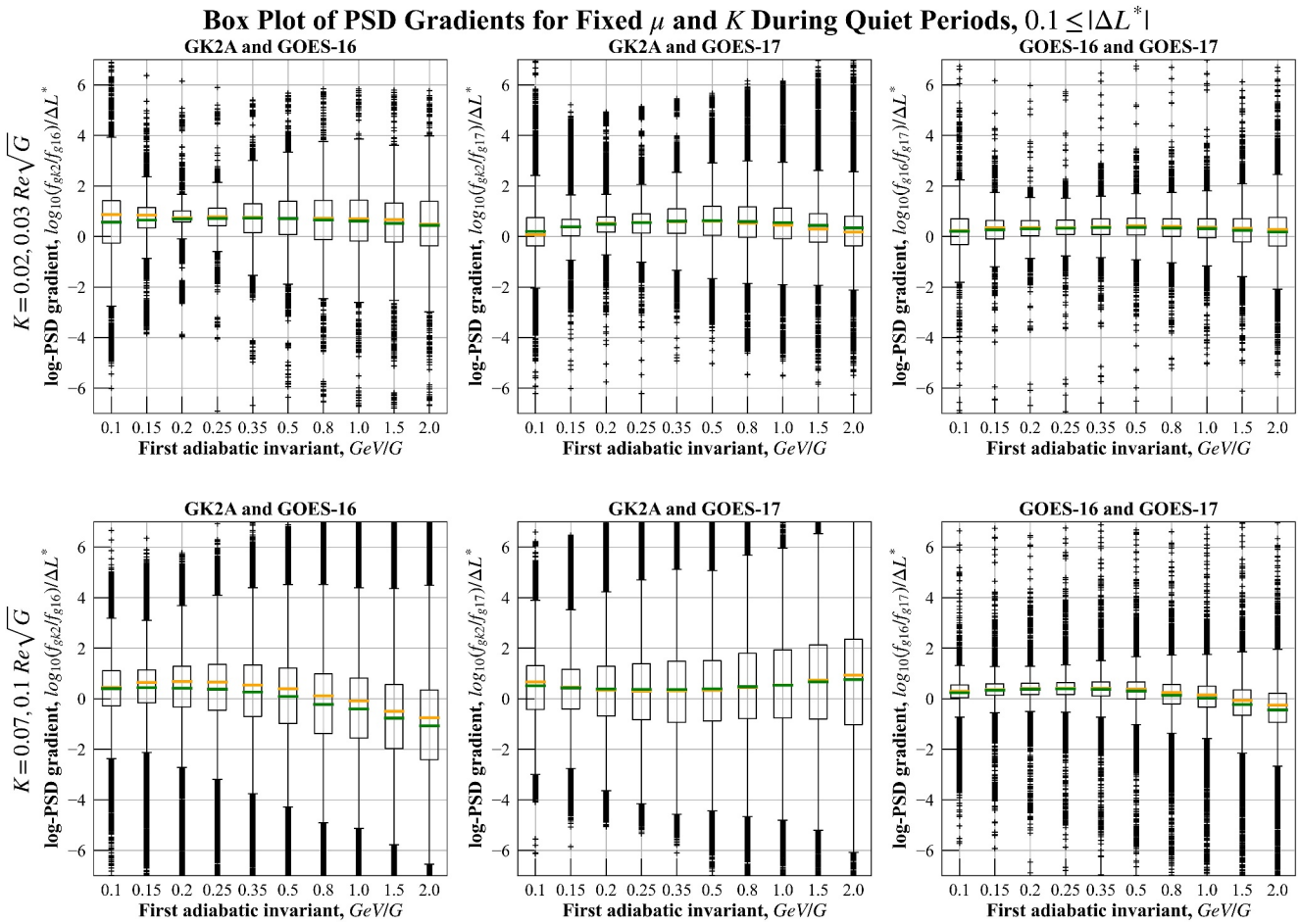

Figure 8. Tendencies of PSD gradients according to first and second adiabatic invariants during geomagnetically quiet periods (from left to right): GK2A and GOES-16, GK2A and GOES-17, GOES-16, and GOES-17. Upper-row panels show PSD gradients at K values of 0.02 and 0.03 $R_E\sqrt{G}$, whereas lower-row panels show those at K values of 0.07 and 0.1 $R_E\sqrt{G}$. Vertical axis denotes PSD gradient defined as $\log_{10}\left(f_1/f_2\right)/\Delta L^*$ to symmetrically illustrate the tendencies; horizontal axis denotes values of first adiabatic invariants. Black solid boxes represent IQRs. Lower and upper bases of each box represent medians of lower and upper halves of PSD gradients, respectively. Solid orange and green lines within boxes represent medians and means, respectively. Whiskers extending from boxes indicate upper and lower limits of PSD gradients. Plus markers indicate outliers. Positive PSD gradients are dominant in near-magnetic equatorial plane. For higher K (lower panels), GK2–G16 and G16–G17 pairs exhibited gradual increases in negative gradients above 0.5 GeV/G, whereas GK2–G17 exhibited the opposite trend.

to greater sample variances in the higher μ range (~0.8−2.0 GeV/G) for larger K = 0.07, 0.1 $R_E\sqrt{G}$. This is reflected in the longer whiskers and greater interquartile ranges (IQR) of the box plots. Further, the distribution of L^* differences for the GK2–G17 data sets is more concentrated around $L^* = 0$ as can be easily inferred from the results of 2D-hitogram in Figure 7, which in turn contribute to the observed larger variances in the radial gradient estimation. It should be noted that the accuracy of electron PSDs for larger K is expected to be lower than those for smaller K values. This is due to the coarse pitch angle resolution and poor coverage of off-equatorial polar angles by the instruments and is similarly observed in our analysis (Kress et al., 2020; Seon et al., 2020). Considering these factors, we tentatively conclude that the observed deviations in the GK2–G17 results are likely due to greater statistical variability rather than representing a true physical phenomenon.

The results in Figure 8 suggest a potential pitch-angle dependence of the radial gradient. The gradient appears positive for large pitch angles (top row) and could become negative for higher μ smaller pitch angles (bottom row). Previous studies have examined pitch-angle-dependent radial diffusion mechanisms (Albert, 1999; K.-C. Kim et al., 2011; Y. Shprits et al., 2007; Y. Y. Shprits et al., 2009; Su et al., 2010). These findings imply that the radial gradient of the electron PSD may indeed depend on pitch angle. This gradient could result from either a local acceleration of relativistic particles at smaller L^* due to obliquely propagating waves or loss of particles at

21699402, 2025, 4, Downloaded from https://agupubs.onlinelibrary.wiley.com/doi/10.1029/2024JA033161, Wiley Online Library on [02/10/2025]. See the Terms and Conditions (https://onlinelibrary.wiley.com/terms-and-conditions) on Wiley Online Library for rules of use; OA articles are governed by the applicable Creative Commons License

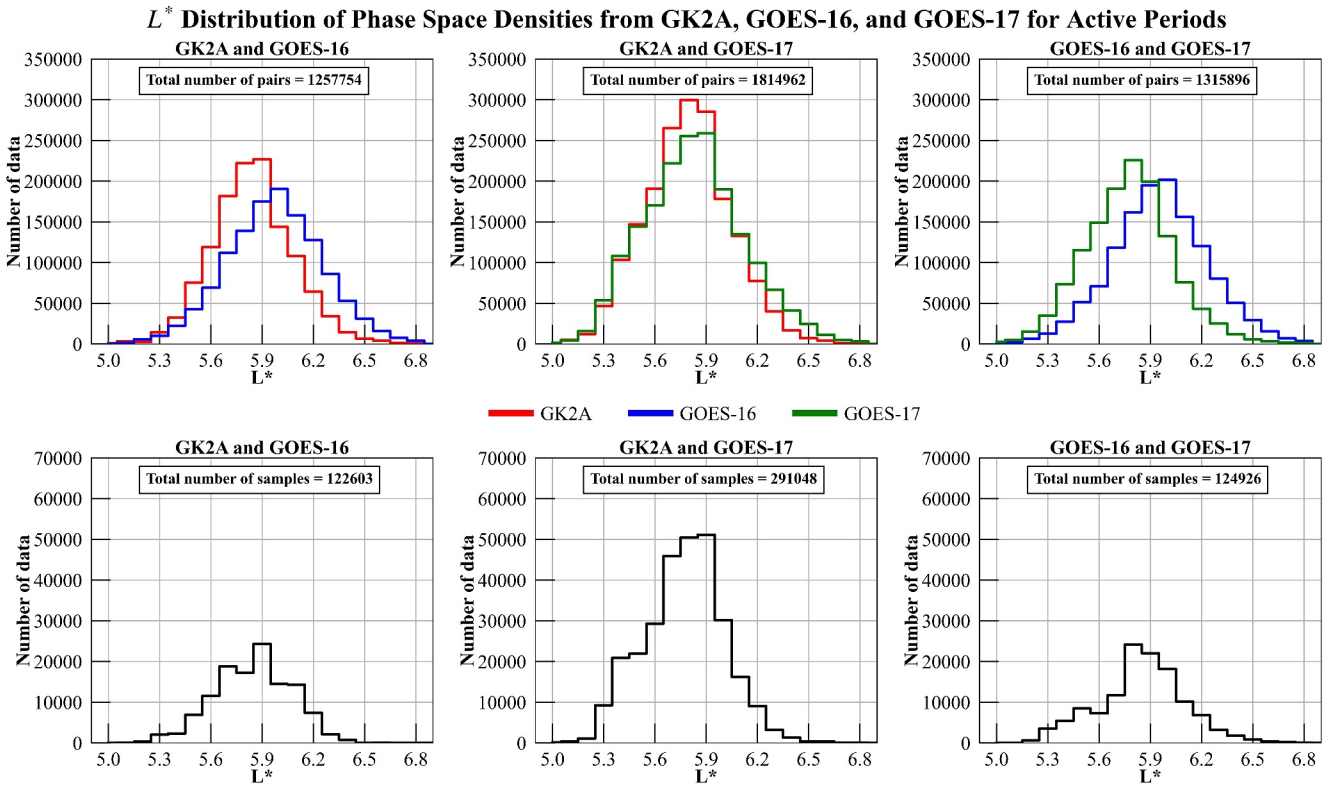

Figure 9. Histograms of L^* values before and after L^* conjunction for geomagnetically active periods. Upper panels present L^* distributions of electron PSDs obtained from the satellites for the same μ, K, and time in geomagnetically active periods. Red, blue, and green indicate GK2A PSDs, GOES-16 PSDs, and GOES-17 PSDs, respectively. Number of PSD pairs for each satellite pair is indicated on top of each upper-row panel. Lower panels summarize results of comparison of electron PSDs at conjunction for the three adiabatic invariants and time. Number of conjunction observations is also indicated in each lower panel. Conjunction of satellites in L^* likely occurred over a wider L^* range compared to in the quiet period.

larger L^* through atmospheric interactions. However, the current analysis does not provide sufficient evidence to identify the precise physical mechanisms responsible for these features. We aim to address these questions through further investigation in future research.

We also investigated the changes in the PSDs for each satellite pair during the active period to perform a comparison between the quiet and active periods. To perform a comparison with the PSDs for geomagnetically active periods, we defined the following set of criteria for the common geomagnetic indices:

$$K_P \geq 3 \text{ or } \mathrm{Dst} \leq -30 \text{ or } \mathrm{AE} \geq 300. \tag{9}$$

It can be observed that the selection of data according to Equation 9 is based on satisfying any of the three geomagnetic indices. By contrast, the conditions in Equation 8 require the simultaneous satisfaction of all three criteria to accurately represent quiet geomagnetic conditions. In formats identical to those of the figures presenting the results for the geomagnetically quiet periods, we provide histograms of L^* values in Figure 9, scatter plots of electron PSDs and histograms of log-PSD ratios in Figure 10, and 2D histograms of PSDs and L^* differences in Figure 11. The plots in the upper row of Figure 9 show the distributions of L^* during the active periods, before the L^* conjunctions between the satellite pairs were implemented. The distribution of L^* was broader, covering a range of 5–7. A trend of GOES-16 traversing larger L^* values than those traversed by GOES-17 and GK2A was also evident from the results. The numbers of available PSD pairs for the satellite pairs are included in the plots. The plots in the bottom row of Figure 9 show the distribution of L^* values after the L^* conjunctions were implemented.

In the same manner as that described in Section 4.3, we attempted cross-satellite calibration based on the values of the electron PSDs to adjust for small offsets existing in the distributions of the PSD ratio for each satellite pair.

21699402, 2025, 4, Downloaded from https://agupubs.onlinelibrary.wiley.com/doi/10.1029/2024JA033161, Wiley Online Library on [02/10/2025]. See the Terms and Conditions (https://onlinelibrary.wiley.com/terms-and-conditions) on Wiley Online Library for rules of use; OA articles are governed by the applicable Creative Commons License

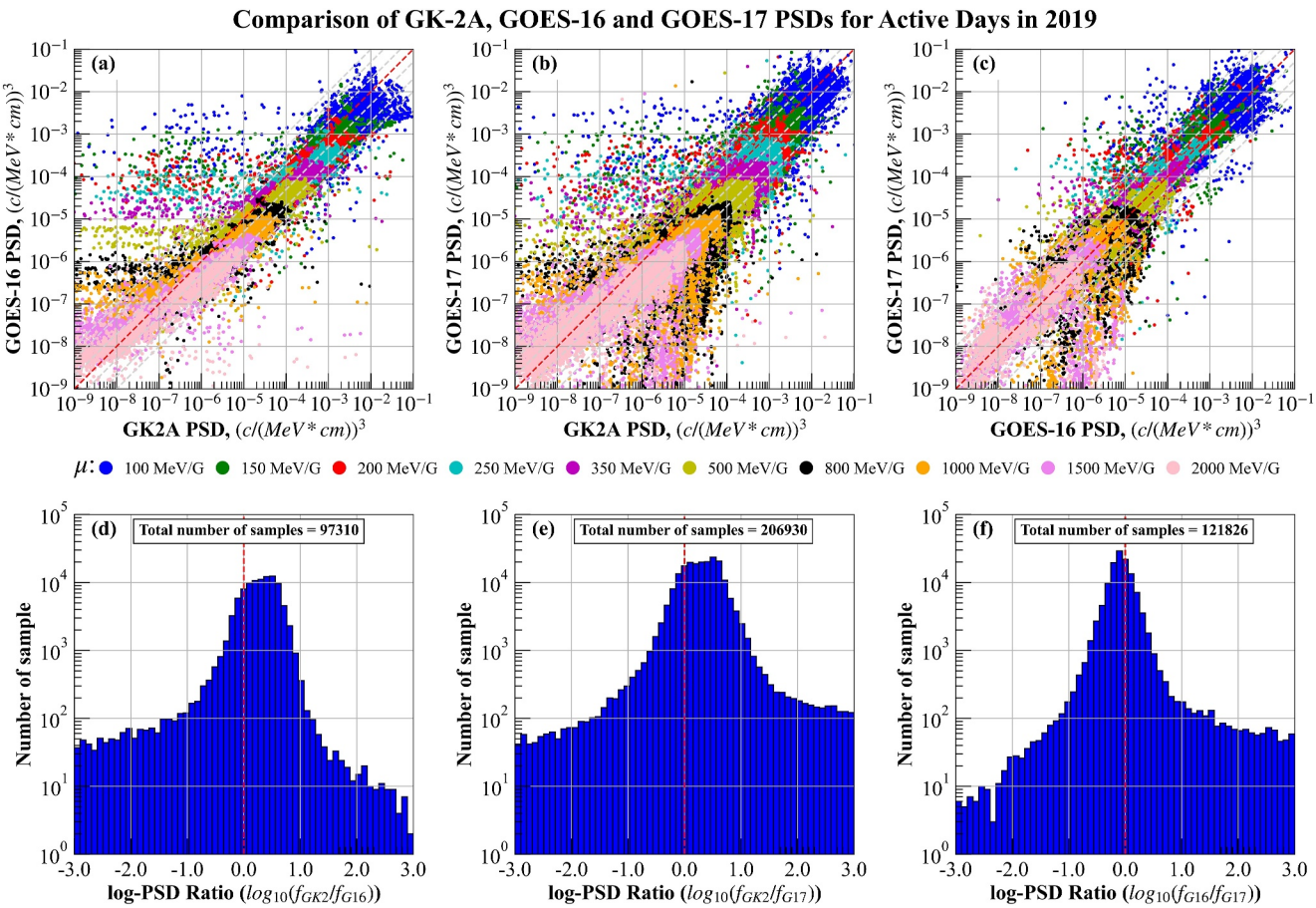

Figure 10. Scatter plots of electron PSDs for geomagnetically active periods (in same format as that of Figures 5 and 6): (a) GK2–G16, (b) GK2–G17, (c) G16–G17; in each scatter plot, marker colors represent first adiabatic invariant values. Histograms of PSD ratios: (d) $\log_{10}\left(f_{GK2}/f_{G16}\right)$, (e) $\log_{10}\left(f_{GK2}/f_{G17}\right)$, (f) $\log_{10}\left(f_{G16}/f_{G17}\right)$. Red dashed lines indicate perfect calibration. Gray dashed lines in (a)–(c) denote PSD ratios of 2, 5, 10, and their inverses, respectively. Peaks of log-PSD ratio distributions in (d)–(f) exhibit significant offsets compared to those in Figure 6.

However, this calibration method may not be applicable during active periods when the PSDs vary significantly. Consequently, for geomagnetically active periods, we performed PSD comparisons without applying inter-satellite PSD calibration. However, we previously confirmed that the PSD ratio is mostly within a factor of ~5 before calibration is applied. As discussed in the following paragraphs, the electron PSDs exhibit significant variability during the active period. The discussion remains applicable regardless of whether or not the PSD calibration factor derived from the quiet days is applied.

Figure 10 shows the scatter plots of the electron PSDs. The data in the figures vividly contrast the PSD differences between the three geostationary satellites, covering a wide range of PSD ratios from 10^{-5} to 10^{5}, which were arbitrarily set to mitigate the influence of outliers. Note that the peaks of the log-PSD ratio distributions in Figure 10 exhibit significant offsets compared to those in Figure 6. This shifting of the peaks away from the previous ratio near zero, along with wider distributions, indicates the existence of larger PSD differences under the same (μ, K, L^*) coordinates. This suggests that during active periods, the assumption of adiabatic invariance is less likely to be valid.

Figure 11 shows two-dimensional histograms of the log-PSD ratios and L^* differences. Positive and negative radial gradients can be observed in the first and third quadrants and the second and fourth quadrants of the histogram plane, respectively. The number of samples is color coded in accordance with the color bar on the right-hand side of each plot. The results of the 2D histograms in the upper row are further summarized in the bottom row by counting the number of gradient signs. The bottom row of Figure 11 displays the frequency of positive and negative gradients during quiet and active periods. The percentage of frequency during quiet periods is

21699402, 2025, 4, Downloaded from https://agupubs.onlinelibrary.wiley.com/doi/10.1029/2024JA033161, Wiley Online Library on [02/10/2025]. See the Terms and Conditions (https://onlinelibrary.wiley.com/terms-and-conditions) on Wiley Online Library for rules of use; OA articles are governed by the applicable Creative Commons License

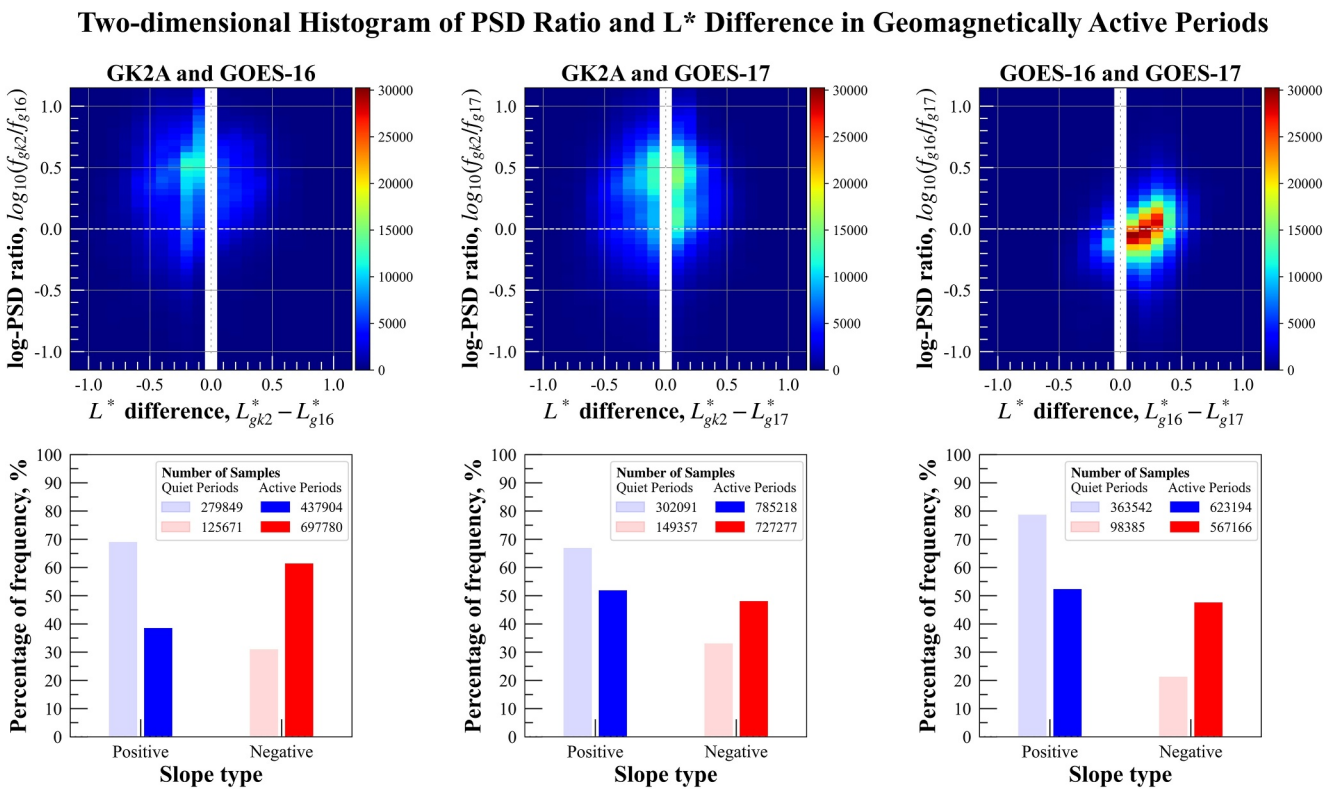

Figure 11. Two-dimensional histograms of log-PSD ratio and L^* difference in geomagnetically active periods (left to right): GK2–G16, GK2–G17, and G16–G17. Upper-row and lower-row panels are depicted in the same manner those of Figure 7. Each upper-row grid of panels represents a log-PSD gradient. First and third quadrants indicate positive gradients; second and fourth quadrants indicate negative gradients. Frequencies are color coded in accordance with right-side color bar of each upper-row panel. L^* difference bins in 0.1 increments account for uncertainties in L^*, whereas log-PSD ratio is represented in logarithmic form of f_1/f_2 to show symmetry around zero. Lower-row panels present frequency percentages of positive and negative slopes for corresponding upper-row panels. Blue represents percentages of samples with positive slopes, whereas red represents those with negative slopes. The translucent bars represent frequency percentages during the quiet periods. The numbers of samples for each category are indicated in the legend. Compared to those in the quiet period, negative gradients have significantly increased, with the GK2–G16 pair even showing a predominant frequency of negative gradients.

represented by translucent bars, while the percentage of frequency during active periods is represented by darker-colored bars. As shown in the bottom row of Figure 11, a comparison of the PSD gradients between quiet and active periods revealed an increase in the occurrence of negative PSD gradients during the active phases. Herein, the GK2–G16 pair exhibited the highest occurrence of negative gradients, whereas for the other two pairs, the occurrence of positive gradients was slightly higher than that of negative gradients. The GK2–G16, GK2–G17, and G16–G17 pairs exhibited decreases in the occurrence of positive gradients during the active period compared to those in the quiet period by approximately 30%, 15%, and 26%, respectively. Conversely, the occurrence of negative gradients increased by 30%, 15%, and 26%, respectively. These results clearly demonstrate the growth of a negative PSD gradient in the active period. Further research is necessary to determine whether this increase in the negative gradients is attributable more to nonadiabatic or to adiabatic processes (see Ripoll et al., 2020 and references therein for details related to the injection, loss, and acceleration of electrons).

For the active periods, a detailed analysis of the log-PSD gradient trend in specific adiabatic coordinates, similar to that shown in Figure 8, was not performed because of the absence of calibration. This analysis is deferred for future research.

We conducted an initial investigation to explore the relationship between solar wind parameters and the radial gradient results. Figure 12 presents histograms illustrating the distributions of geomagnetic indices and key solar wind parameters. The top row of Figure 12 summarizes the distributions of geomagnetic indices, K_P, Dst, and AE, while the bottom row shows the distributions of the solar wind speed (V_{sw}), dynamic pressure (P_{dyn}), and the z-component of the interplanetary magnetic field (IMF B_z) during the quiet and active periods. In each panel, blue dashed line represents the entire period without imposing any geomagnetic conditions, green dashed line

21699402, 2025, 4, Downloaded from https://agupubs.onlinelibrary.wiley.com/doi/10.1029/2024JA033161, Wiley Online Library on [02/10/2025]. See the Terms and Conditions (https://onlinelibrary.wiley.com/terms-and-conditions) on Wiley Online Library for rules of use; OA articles are governed by the applicable Creative Commons License

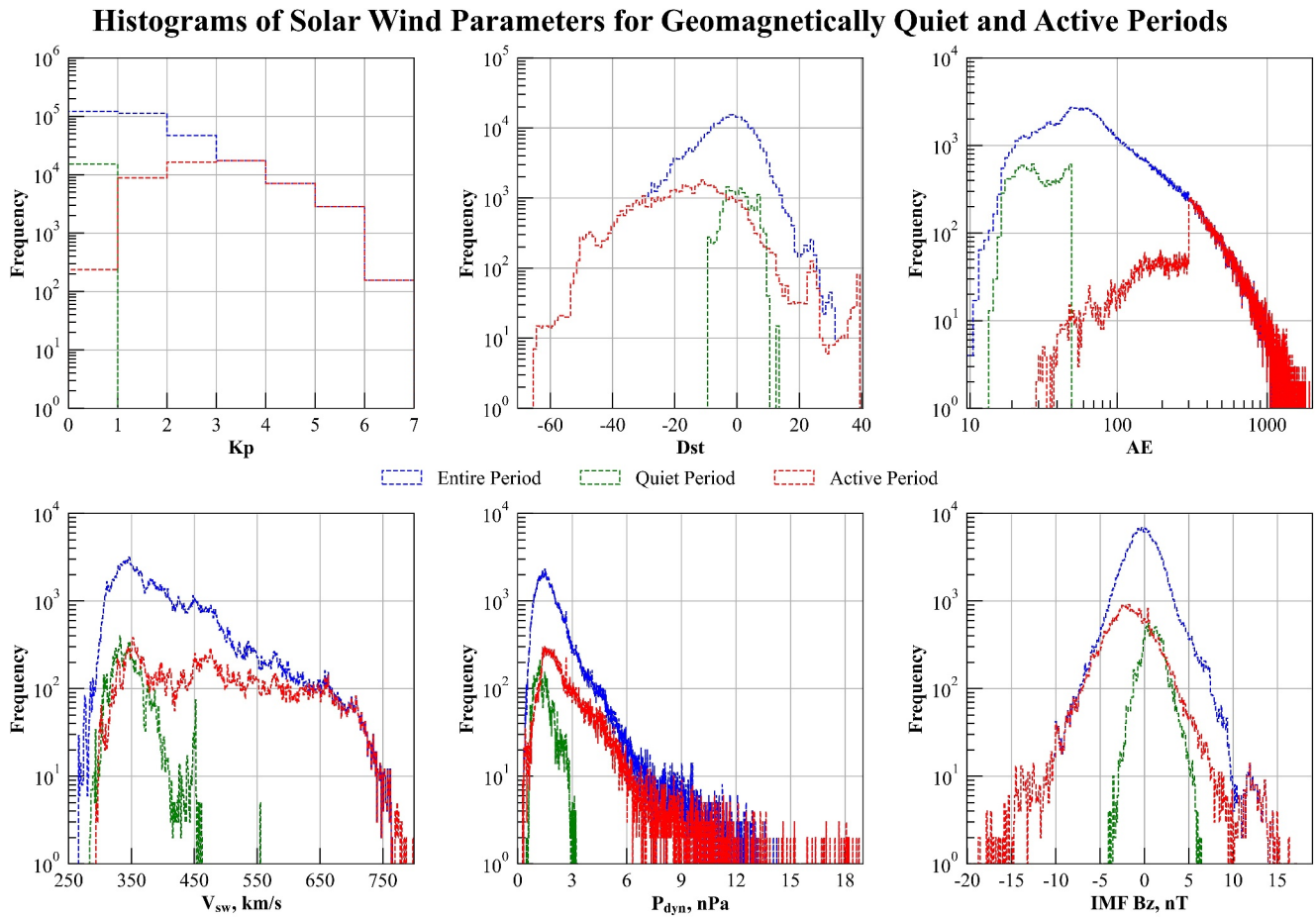

Figure 12. Histograms of geomagnetic indices and solar wind parameters during geomagnetically quiet and active periods. The top row shows the distributions of the Dst, K_P, and AE index, while the bottom row displays the distributions of solar wind parameters: solar wind speed (V_{sw}), dynamic pressure (P_{dyn}), and the z-component of the interplanetary magnetic field (IMF B_Z). The blue dashed lines represent the entire period, the green dashed lines correspond to the quiet period, and the red dashed lines correspond to the active period. The distribution of solar wind parameters during the active period extends over a wider range compared to the quiet period, indicating increased variability in the solar wind during active periods.

represents the quiet period, and red dashed line represents the active period, respectively. As shown in the figure, the distribution of solar wind parameters during the active period includes the distribution of the quiet period and extends over a broader range. The results further confirm that radial gradient estimates during quiet periods are not affected by large Dst values, which are typically associated with sudden storm commencements. The results also show that the solar wind speed, the dynamic pressure, and the magnitude of B_z are considerably smaller during the quiet periods compared to the active periods. We acknowledge that investigating the role of solar wind parameters in the transport, acceleration, and loss processes of the outer radiation belt lies beyond the scope of this study and will be addressed in future research.

Finally, we acknowledge that our analysis in this study is based on several assumptions that require further investigation. In calculating the electron PSDs, as detailed in Section 3 (PSD Calculation in Invariant Coordinates), the first adiabatic invariant (μ) was estimated with the measured local magnetic field. However, other quantities, such as the second adiabatic invariant (K), the equatorial pitch angle (B_{eq}) and the third adiabatic invariant (L^*), rely on global magnetic field models. This introduces a question of whether the combination of measured and model magnetic fields impacts the results. Although it was assumed that using actual measurements to estimate μ would enhance the analysis, the impact of using measured versus modeled magnetic fields on μ needs further investigation for clarification. In addition, the effect of different global magnetic field models should be assessed, as only TS05 model (Tsyganenko & Sitnov, 2005) was considered in this study.

21699402, 2025, 4, Downloaded from https://agupubs.onlinelibrary.wiley.com/doi/10.1029/2024JA033161, Wiley Online Library on [02/10/2025]. See the Terms and Conditions (https://onlinelibrary.wiley.com/terms-and-conditions) on Wiley Online Library for rules of use; OA articles are governed by the applicable Creative Commons License

21699402, 2025, 4, Downloaded from https://agupubs.onlinelibrary.wiley.com/doi/10.1029/2024JA033161, Wiley Online Library on [02/10/2025]. See the Terms and Conditions (https://onlinelibrary.wiley.com/terms-and-conditions) on Wiley Online Library for rules of use; OA articles are governed by the applicable Creative Commons License

The results presented were obtained from instruments with limited pitch angle resolution due to the satellite's fixed orientation relative to the Earth's surface. This contrasts with instruments aboard spinning satellites, which offer better pitch angle resolution. In the present study, each energy bin for the calculated PSDs in the present study has only five or six measurements available against the pitch angles for GOES or GK2A, respectively. Due to the limited number of pitch angle measurements, a simple function with just two fitting parameters (see Equation 7) was used to describe the PAD, as detailed in Section 3. While this simplified function may model monotonically decreasing PADs with a peak electron flux at 90° (Gannon et al., 2007; Gu et al., 2011; Vampola, 1997), it may not properly account for more complex flattop or butterfly-shaped PADs observed in the outer radiation belt (Artemyev et al., 2015; Medeiros et al., 2019; Sibeck et al., 1987; Su et al., 2010; West et al., 1973; Xiao et al., 2015) that are occasionally observed during geomagnetically active periods. These studies have identified various factors that influence the shape of the PAD, including wave-particle interactions, shell-splitting, and magnetopause shadowing, which depend on electron kinetic energy, magnetic local time, and geomagnetic activity.

This study investigated the broad statistical trends in relation to geomagnetic indices. For example, Figures 7 and 11 summarize the observed variations in electron PSDs for all μ and K, categorizing events into geomagnetically quiet and active phases. A more detailed examination of the electron PSD gradients for small and large pitch angles, shown in the upper and lower panels of Figure 8, respectively, suggests that the radial gradient may depend on electron energy and pitch angle. There is a tendency for larger radial gradients near μ values of 350–500 MeV/G, while smaller gradients are observed for μ values below 200 MeV/G and above 1,000 MeV/G. This tendency toward smaller radial gradients at lower and higher μ appears to be more pronounced for larger pitch angles, as shown in the lower panels of Figure 8. However, the support for this trend is weaker from the GK2A-GOES-17 observation (lower center panel). It remains unclear whether this is due to increased numerical fluctuations at larger K s (smaller pitch angles), which may result from the oversimplified functional form of the PADs based on the coarse pitch angle resolutions.

6. Conclusion

In this study, we compared the PSDs between pairs of geostationary satellites during geomagnetically quiet and active periods. Through cross-satellite calibration utilizing conjunction observations during geomagnetically quiet periods, we obtained a more accurate PSD radial gradient between geostationary satellites. These gradients can be calculated based on the different magnetic latitudes and the subsequent traversal of different L^* values by the three geostationary satellites. The radial gradient of the PSDs, inferred from variations along the third adiabatic invariant L^*, is closely linked to electron injection, transport, acceleration, and loss processes within the radiation belt.

Our findings indicated that during geomagnetically quiet periods, there is a predominance of positive PSD gradients near geostationary orbits, particularly in the near-magnetic equatorial plane. For electrons moving to further latitudes, the GK2–G16 and G16–G17 pairs exhibited increases in negative gradients above 0.5 GeV/G, whereas the GK2–G17 pair showed an increase in positive gradients.

During the geomagnetically active periods, the GK2–G16, GK2–G17, and G16–G17 pairs showed decreases in positive gradients by approximately 30%, 15%, and 26%, respectively, compared to those in the quiet period. Conversely, the occurrence of negative gradients increased by approximately 30%, 15%, and 26%, respectively. These findings indicate the growth of a negative PSD gradient during active periods. However, because this study focused more on comparing the PSDs measured by the three satellites during quiet periods, the mechanisms by which the negative gradient becomes more frequent during active periods will be addressed in future research.

Our study has some limitations, including the pitch angle resolution and error of the magnetic field model. The pitch angle resolution of differential flux measurements from geostationary satellites is quite low because of the small number of telescopes and poor coverage of polar angles. The TS05 model was used to simulate the global magnetic field, and the impact of magnetic field errors on PSD and adiabatic invariant calculations was not quantitatively analyzed. In the future, we will include other spinning satellites to address the pitch angle resolution problem and consider magnetic field model errors in PSDs and invariants.

Appendix A: Uncertainty in Electron PSD

The uncertainty of the electron phase space density (PSD) can be estimated from the uncertainty of the electron differential flux by performing a procedure similar to that for the PSD calculation. As shown in Figure 2, first, we should determine the equatorial pitch angle α_K corresponding to the desired second adiabatic invariant K. To compute α_K, a curve fitting procedure is employed wherein an analytic function is fitted to 15 pairs of α_K, for a given K, obtained from the global geomagnetic field model of the International Radiation Belt Environment Modeling (IRBEM) module in SpacePy. The specific fitting function is shown in panel (2) of Figure 2. It should be noted that uncertainties in the global magnetic field model and the desired K are disregarded throughout the calculation of the uncertainty. Thus, the uncertainty associated with α_K, denoted as $\delta\alpha_K$, is assumed to be zero.

In the second step, it is necessary to deduce the differential flux corresponding to α_K from a pitch angle distribution (PAD). This distribution can be obtained from satellite measurements. The satellite measurements used in this study provided multiple pitch-angle-resolved differential fluxes, which were facilitated by instruments equipped with several particle detectors focused in various directions to encompass the entire pitch angle range. As illustrated in panel (3-A) of Figure 2, we assume the PAD to be as defined in Equation A1 and subsequently apply a suitable curve fitting process to match Equation A1 with the observed differential fluxes.

$$J_E = C_4 \sin^n \alpha_K, \tag{A1}$$

where J_E is the differential flux, and C_4 and n are the fitting parameters. Equation A1 is identical to Equation 7 in Section 3; however, we append the subscript E to the flux J in Equation A1 to explicitly indicate that the energy of the differential flux is fixed at the current calculation step.

The least squares fitting of the PAD requires several pitch-angle-resolved differential fluxes and the uncertainties in the fluxes. We used the differential fluxes and corresponding uncertainties measured by the satellite. These uncertainties, inherent to the differential fluxes, consist of a Poisson error, which is represented as the square root of the count $(\sqrt{N})$, and a systematic error. The yields of the least squares fitting are the optimal fitting parameter values and a covariance matrix that includes information on the uncertainties of the parameters.

From the uncertainty propagation formula and the assumption that is $\delta\alpha_K = 0$, the uncertainty of differential flux at the given second adiabatic invariant (or the given equatorial pitch angle α_K) can be expressed as Equation A2:

$$(\delta J_E)^2 = (\delta J_E(C_4, n))^2 = \sum_{i,j=1}^{2} \frac{\partial J_E}{\partial X_i}\frac{\partial J_E}{\partial X_j}\delta X_i \delta X_j \text{ with } X_1 = C_4 \text{ and } X_2 = n. \tag{A2}$$

The partial derivatives of J_E are defined in Equation A3, and the uncertainties in the fitting parameters $\delta X_i \delta X_j$ are obtained from the covariance matrix yielded by the least squares fitting of the PAD.

$$\begin{aligned} \frac{\partial J_E}{\partial C_4} &= \sin^n \alpha_K \\ \frac{\partial J_E}{\partial n} &= J(\alpha_K)\log(\sin \alpha_K) \end{aligned} \tag{A3}$$

Next, we calculate the uncertainty of the differential flux for the given first and second adiabatic invariants. To calculate this uncertainty, we should create an energy spectrum using the aforementioned J_E and then determine the specific energy corresponding to the first adiabatic invariants.

As shown in panel (3-B) in Figure 2, we can determine the energy corresponding to the given first adiabatic invariant (E_μ) from the definition of the magnetic moment of a gyrating particle with α_K. In this study, we also assume that the uncertainty related to the energy bin width (δE) is zero. Therefore, the uncertainty of the energy corresponding to the given first adiabatic invariant (δE_μ) is zero.

By iterating the calculation of Equations A1 and A2 for all energy bins, we can obtain an energy spectrum for the given K, as shown in panel (4) of Figure 2, and the corresponding uncertainties. In this analysis, we fit the kappa

21699402, 2025, 4, Downloaded from https://agupubs.onlinelibrary.wiley.com/doi/10.1029/2024JA033161, Wiley Online Library on [02/10/2025]. See the Terms and Conditions (https://onlinelibrary.wiley.com/terms-and-conditions) on Wiley Online Library for rules of use; OA articles are governed by the applicable Creative Commons License

distribution to the energy spectrum. For the fitting with the kappa distribution, we simplify the exact kappa distribution, as shown in Equation A4:

$$J = p_1 \cdot E \cdot \left(1 + E/p_2\right)^{-\left(1+p_3\right)}, \tag{A4}$$

where $p_1, p_2,$ and p_3 are the fitting parameters.

In the same manner as in Equation A2, the uncertainty of the differential flux can be expressed as Equation A5. The uncertainty of the differential flux (δJ) includes both uncertainties originating from the fittings of PAD and energy spectrum.

$$(\delta J)^2 = \sum_{i,j=1}^{3} \left(\frac{\partial J}{\partial p_i}\right)\left(\frac{\partial J}{\partial p_j}\right)\delta p_i \delta p_j \tag{A5}$$

The partial derivatives of J with respect to $p_1, p_2,$ and p_3 are shown in Equation A6. From the covariance matrix yielded by the fitting of the energy spectrum, we can obtain $\delta p_i \delta p_j$.

$$\begin{aligned} \frac{\partial J}{\partial p_1} &= E\left(1 + E/p_2\right)^{-\left(1+p_3\right)} \\ \frac{\partial J}{\partial p_2} &= \frac{p_1\left(1+p_3\right)E^2\left(1+E/p_2\right)^{-p_3}}{\left(E+p_2\right)^2} \\ \frac{\partial J}{\partial p_3} &= -J\log\left(1 + E/p_2\right) \end{aligned} \tag{A6}$$

The PSD can be expressed as Equation A7.

$$f = \frac{J}{\left(E^2 + 2m_0c^2E\right)}, \tag{A7}$$

where f is the electron PSD, m_0 is the rest mass of an electron, and c is the speed of light.

Because we assume that δE is zero, the uncertainty of the PSD can be described in a simple manner using the propagation formula provided in Equation A8:

$$(\delta f)^2 = \left(\frac{\partial f}{\partial J}\right)^2 (\delta J)^2. \tag{A8}$$

The partial derivative of the PSD with respect to J is shown in Equation A9:

$$\frac{\partial f}{\partial J} = \frac{1}{\left(E^2 + 2m_0c^2E\right)}. \tag{A9}$$

Finally, the uncertainty of the electron PSD for the given first and second adiabatic invariants is expressed by Equation A10:

$$(\delta f(\mu, K))^2 = \left(\frac{1}{\left(E^2 + 2m_0c^2E\right)}\right)^2 (\delta J)^2. \tag{A10}$$

Appendix B: Uncertainty in L^*

The L^* value, directly related to the third adiabatic invariant, the magnetic flux $\Phi = \oint B \cdot \mathrm{dS}$ in Equation 3, requires computationally intensive calculations. Determining L^* inherently relies on a global geomagnetic model

21699402, 2025, 4, Downloaded from https://agupubs.onlinelibrary.wiley.com/doi/10.1029/2024JA033161, Wiley Online Library on [02/10/2025]. See the Terms and Conditions (https://onlinelibrary.wiley.com/terms-and-conditions) on Wiley Online Library for rules of use; OA articles are governed by the applicable Creative Commons License

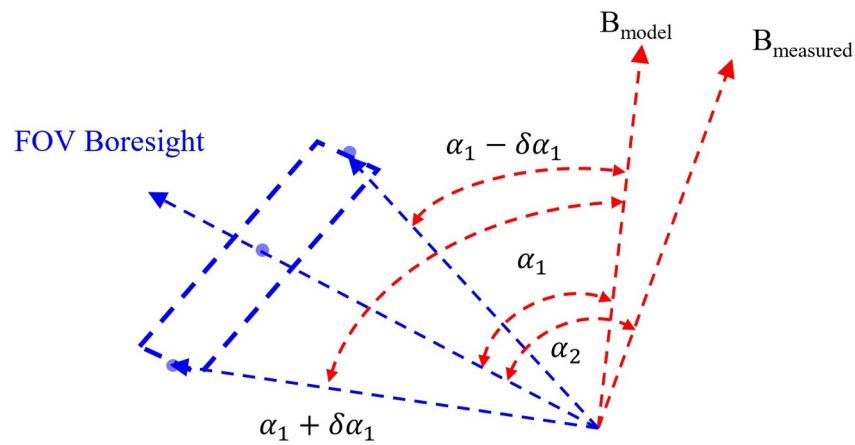

Figure B1. Illustration of uncertainties in pitch angle between local magnetic field and instrument field of view (FOV). When third adiabatic invariant L^* is calculated, uncertainty in the pitch angle estimate introduces a corresponding uncertainty in L^*. This uncertainty can stem from magnetic field vectors, which may be derived from direct measurements or a magnetic field model, leading to uncertainty denoted as ΔL_1^*. Additionally, finite size of the instrument's FOV introduces uncertainties in the velocity vector of measured differential fluxes, further contributing to pitch angle estimate uncertainty, denoted as ΔL_2^*. Final estimate in the present study, denoted as ΔL^*, is obtained from relation $\Delta L^* = \sqrt{(\Delta L_1^*)^2 + (\Delta L_2^*)^2}$.

to trace charged particles along complete drift shells within the magnetic field and to compute the magnetic flux Φ along these shells. Numerous factors can contribute to uncertainties in L^*, including the accuracies of the input solar wind parameters and temporal resolutions, choice of the global magnetic field model and levels of geomagnetic activity, and numerical algorithm used for the drift shell tracing. Estimating the L^* uncertainty while considering these factors poses a formidable computational challenge. However, the propagation of these uncertainty factors through our nonlinear calculations to provide a reasonable estimate for L^* remains unclear. In this study, only the following specific factors were taken into account in deriving approximate estimates of the L^* magnitudes, recognizing the dependence of the L^* value on the pitch angle at the satellite's position:

1. The differential flux of the electrons, used to calculate the PSD according to Equation 1, was assumed to have a pitch angle by assigning a velocity direction along the boresight of each electron telescope with respect to the local magnetic field. The finite size of the FOV for each telescope, approximately ±15° for GK2A and ±20° for the GOES satellites, introduces uncertainty to the pitch angle α ($\alpha_1 \pm \delta\alpha_1$ in Figure B1).
2. Two independent estimates of the pitch angle are possible from two local magnetic field vectors: one derived from the employed magnetic field model and the other measured by the magnetometer. Note that the three geostationary satellites acquired continuous measurements of geomagnetic fields. Differences in these estimates of the pitch angles lead to variations in the estimated L^* values (α_1 and α_2 in Figure B1).

When the third adiabatic invariant L^* is calculated, the uncertainty in the pitch angle estimate, contributed by the two aforementioned factors, introduces a corresponding uncertainty in L^*. This uncertainty can stem from the magnetic field vectors, which may be derived from direct measurements or a magnetic field model, leading to an uncertainty (denoted as ΔL_1^*). Additionally, the finite size of the instrument's FOV introduces uncertainties in the velocity vector of the measured differential fluxes, further contributing to the pitch angle estimate uncertainty (denoted as ΔL_2^*). The final estimate in the present study, denoted as ΔL^*, is obtained from the relation $\Delta L^* = \sqrt{(\Delta L_1^*)^2 + (\Delta L_2^*)^2}$. We have calculated ΔL^* at 1-min cadence for the entire duration of this study, from 2 May to 20 November 2019, for all telescopes of the three satellites. Analysis of the distribution of the calculated ΔL^* suggested that selecting $\Delta L^* = 0.1$ would yield a reasonable estimate for the uncertainty in L^*, associated with the uncertainties of the pitch angles as previously explained. This is because approximately 89.9%, 69.9%, and 73.5% of the ΔL^* samples fall below $\Delta L^* = 0.1$ for GK2A, GOES-16, and GOES-17, respectively, during the period examined in this study.

21699402, 2025, 4, Downloaded from https://agupubs.onlinelibrary.wiley.com/doi/10.1029/2024JA033161, Wiley Online Library on [02/10/2025]. See the Terms and Conditions (https://onlinelibrary.wiley.com/terms-and-conditions) on Wiley Online Library for rules of use; OA articles are governed by the applicable Creative Commons License

Data Availability Statement

Data—The GK2A KSEM level-1 electron flux data prior to the implementation of the findings of this research are available at National Meteorological Satellite Center of the Korea Meteorological Administration via the National Data Service Repository (https://datasvc.nmsc.kma.go.kr/).

Data—The GOES-16 and GOES-17 level-2 electron flux data were obtained from the National Centers for Environmental Information of NOAA (https://www.ngdc.noaa.gov/stp/satellite/goes-r.html).

Data—The input parameters for the TS05 magnetic field model, derived from OMNIWeb data, were provided by Zhengui Qin and Richard Denton. These parameters are available at the Integrated Space Weather Analysis (ISWA) Data Tree developed by the Community Coordinated Modeling Center (CCMC) at NASA's Goddard Space Flight Center (https://iswa.ccmc.gsfc.nasa.gov/iswa_data_tree/composite/magnetosphere/Qin-Denton/1min/).

Data—The OMNI data for the solar wind and geomagnetic index were obtained from the Space Physics Data Facility of NASA (https://spdf.gsfc.nasa.gov/).

Software—SpacePy 0.4.1 used for calculating adiabatic invariants and geomagnetic field model outputs is preserved at https://doi.org/10.5281/zenodo.3252523, available via Zenodo (Morley et al., 2024).

Software—IRBEM (5.0.0) utilized in SpacePy 0.4.1 for magnetic field modeling and particle trajectory calculations is preserved at https://doi.org/10.5281/zenodo.6867552, available via Zenodo (Boscher et al., 2022).

Acknowledgments
The Korean authors wish to acknowledge the support provided by the Korea Aerospace Research Institute (KARI) and National Meteorological Satellite Center (NMSC) throughout the project. Part of this work was supported by the National Research Foundation (Grant NRF-2020M1A3B7109195) and Institute of Information and Communication Technology Planning and Evaluation (Grant RS-2024-00398716) funded by the Ministry of Science and ICT of Korea. The research at the University of Colorado CIRES was supported by NOAA cooperative agreement NA22OAR4320151. The statements, findings, conclusions, and recommendations are those of the authors and do not necessarily reflect the views of NOAA or the U.S. Department of Commerce.

References

Albert, J. M. (1999). Analysis of quasi-linear diffusion coefficients. *Journal of Geophysical Research*, *104*(A2), 2429–2441. https://doi.org/10.1029/1998JA900113

Arnoldy, R. L., & Chan, K. W. (1969). Particle substorms observed at the geostationary orbit. *Journal of Geophysical Research*, *74*(21), 5019–5028. https://doi.org/10.1029/JA074i021p05019

Artemyev, A. V., Agapitov, O. V., Mozer, F. S., & Spence, H. (2015). Butterfly pitch angle distribution of relativistic electrons in the outer radiation belt: Evidence of nonadiabatic scattering. *Journal of Geophysical Research: Space Physics*, *120*(6), 4279–4297. https://doi.org/10.1002/2014JA020865

Baker, D. N., Higbie, P. R., Hones, E. W., & Belian, R. D. (1978). High-resolution energetic particle measurements at 6.6 R_E 3. Low-energy electron anisotropies and short-term substorm predictions. *Journal of Geophysical Research*, *83*(A10), 4863–4868. https://doi.org/10.1029/JA083iA10p04863

Belian, R. D., Cayton, T. E., Christensen, R. A., Ingraham, J. C., Meier, M. M., Reeves, G. D., & Lazarus, A. J. (1996). Relativistic electrons in the outer-zone: An 11 year cycle; Their relation to the solar wind. In *AIP Conference Proceedings* (Vol. 383, pp. 13–18). https://doi.org/10.1063/1.51526

Boggs, P. T., & Rogers, J. E. (1990). Orthogonal distance regression. *Contemporary Mathematics*, *112*, 183–194. https://doi.org/10.1090/conm/112/1087109

Bogott, F. H., & Mozer, F. S. (1973). Nightside energetic particle decreases at the synchronous orbit. *Journal of Geophysical Research*, *78*(34), 8119–8127. https://doi.org/10.1029/JA078i034p08119

Boscher, D., Bourdarie, S., O'Brien, P., Guild, T., Heynderickx, D., Morley, S., et al. IRBEM Contributor Community. (2022). PRBEM/IRBEM: V5.0.0 (version IRBEM-5.0.0) [Computer software]. *Zenodo*. https://doi.org/10.5281/ZENODO.6867552

Boudouridis, A., Rodriguez, J. V., Kress, B. T., Dichter, B. K., & Onsager, T. G. (2020). Development of a bowtie inversion technique for real-time processing of the GOES-16/-17 SEISS MPS-HI electron channels. *Space Weather*, *18*(4), e2019SW002403. https://doi.org/10.1029/2019SW002403

Boyd, A. J., Spence, H. E., Claudepierre, S. G., Fennell, J. F., Blake, J. B., Baker, D. N., et al. (2014). Quantifying the radiation belt seed population in the 17 March 2013 electron acceleration event. *Geophysical Research Letters*, *41*(7), 2275–2281. https://doi.org/10.1002/2014GL059626

Chen, Y., Friedel, R. H. W., Reeves, G. D., Cayton, T. E., & Christensen, R. (2007). Multisatellite determination of the relativistic electron phase space density at geosynchronous orbit: An integrated investigation during geomagnetic storm times. *Journal of Geophysical Research*, *112*(A11), 2007JA012314. https://doi.org/10.1029/2007JA012314

Chen, Y., Friedel, R. H. W., Reeves, G. D., Onsager, T. G., & Thomsen, M. F. (2005). Multisatellite determination of the relativistic electron phase space density at geosynchronous orbit: Methodology and results during geomagnetically quiet times. *Journal of Geophysical Research*, *110*(A10), 2004JA010895. https://doi.org/10.1029/2004JA010895

Dichter, B. K., Galica, G. E., McGarity, J. O., Tsui, S., Golightly, M. J., Lopate, C., & Connell, J. J. (2015). Specification, design, and calibration of the space weather suite of instruments on the NOAA GOES-R program spacecraft. *IEEE Transactions on Nuclear Science*, *62*(6), 2776–2783. https://doi.org/10.1109/TNS.2015.2477997

Friedel, R. H. W., Bourdarie, S., & Cayton, T. E. (2005). Intercalibration of magnetospheric energetic electron data. *Space Weather*, *3*(9), 2005SW000153. https://doi.org/10.1029/2005SW000153

Gannon, J. L., Li, X., & Heynderickx, D. (2007). Pitch angle distribution analysis of radiation belt electrons based on Combined Release and Radiation Effects Satellite Medium Electrons A data. *Journal of Geophysical Research*, *112*(A5), 2005JA011565. https://doi.org/10.1029/2005JA011565

Green, J. C., & Kivelson, M. G. (2001). A tale of two theories: How the adiabatic response and ULF waves affect relativistic electrons. *Journal of Geophysical Research*, *106*(A11), 25777–25791. https://doi.org/10.1029/2001JA000054

21699402, 2025, 4, Downloaded from https://agupubs.onlinelibrary.wiley.com/doi/10.1029/2024JA033161, Wiley Online Library on [02/10/2025]. See the Terms and Conditions (https://onlinelibrary.wiley.com/terms-and-conditions) on Wiley Online Library for rules of use; OA articles are governed by the applicable Creative Commons License

Green, J. C., & Kivelson, M. G. (2004). Relativistic electrons in the outer radiation belt: Differentiating between acceleration mechanisms. *Journal of Geophysical Research*, *109*(A3), 2003JA010153. https://doi.org/10.1029/2003JA010153

Gu, X., Zhao, Z., Ni, B., Shprits, Y., & Zhou, C. (2011). Statistical analysis of pitch angle distribution of radiation belt energetic electrons near the geostationary orbit: CRRES observations: Radiation belt energetic electron PAD. *Journal of Geophysical Research*, *116*(A1), A01208. https://doi.org/10.1029/2010JA016052

Higbie, P. R., Belian, R. D., & Baker, D. N. (1978). High-resolution energetic particle measurements at 6.6 R_E, 1. Electron micropulsations. *Journal of Geophysical Research*, *83*(A10), 4851–4855. https://doi.org/10.1029/JA083iA10p04851

Iles, R. H. A., Meredith, N. P., Fazakerley, A. N., & Horne, R. B. (2006). Phase space density analysis of the outer radiation belt energetic electron dynamics. *Journal of Geophysical Research*, *111*(A3), 2005JA011206. https://doi.org/10.1029/2005JA011206

Joselyn, J. A. (1989). Geomagnetic quiet day selection. *Pure and Applied Geophysics PAGEOPH*, *131*(3), 333–341. https://doi.org/10.1007/BF00876832

Kalliokoski, M. M. H., Kilpua, E. K. J., Osmane, A., Jaynes, A. N., Turner, D. L., George, H., et al. (2022). Phase space density analysis of outer radiation belt electron energization and loss during geoeffective and nongeoeffective sheath regions. *Journal of Geophysical Research: Space Physics*, *127*(3), e2021JA029662. https://doi.org/10.1029/2021JA029662

Kim, H., & Chan, A. A. (1997). Fully adiabatic changes in storm time relativistic electron fluxes. *Journal of Geophysical Research*, *102*(A10), 22107–22116. https://doi.org/10.1029/97JA01814

Kim, H.-J., Zesta, E., Kim, K.-C., Shprits, Y., Shi, Y., & Lyons, L. R. (2010). Estimation of radial gradients of phase space density from POLAR observations during a quiet period prior to a sudden solar wind dynamic pressure enhancement. *Journal of Geophysical Research*, *115*(A12), 2010JA015722. https://doi.org/10.1029/2010JA015722

Kim, K.-C., Shprits, Y., Subbotin, D., & Ni, B. (2011). Understanding the dynamic evolution of the relativistic electron slot region including radial and pitch angle diffusion: Brief report. *Journal of Geophysical Research*, *116*(A10), A10214. https://doi.org/10.1029/2011JA016684

Koller, J., Reeves, G. D., & Friedel, R. H. W. (2009). LANL* V1.0: A radiation belt drift shell model suitable for real-time and reanalysis applications. *Geoscientific Model Development*, *2*(2), 113–122. https://doi.org/10.5194/gmd-2-113-2009

Koller, J., & Zaharia, S. (2011). LANL* V2.0: Global modeling and validation. *Geoscientific Model Development*, *4*(3), 669–675. https://doi.org/10.5194/gmd-4-669-2011

Kress, B. T., Rodriguez, J. V., & Onsager, T. G. (2020). The GOES-R space environment in Situ suite (SEISS): Measurement of energetic particles in geospace. In *The GOES-R series* (pp. 243–250). Elsevier. https://doi.org/10.1016/B978-0-12-814327-8.00020-2

Lezniak, T. W., & Winckler, J. R. (1970). Experimental study of magnetospheric motions and the acceleration of energetic electrons during substorms. *Journal of Geophysical Research*, *75*(34), 7075–7098. https://doi.org/10.1029/JA075i034p07075

Li, W., & Hudson, M. K. (2019). Earth's van allen radiation belts: From discovery to the van allen Probes era. *Journal of Geophysical Research: Space Physics*, *124*(11), 8319–8351. https://doi.org/10.1029/2018JA025940

Li, X., Baker, D. N., Teremin, M., Cayton, T. E., Reeves, G. D., Selesnick, R. S., et al. (1999). Rapid enchancements of relativistic electrons deep in the magnetosphere during the May 15, 1997, magnetic storm. *Journal of Geophysical Research*, *104*(A3), 4467–4476. https://doi.org/10.1029/1998JA900092

Liu, Z.-Y., Zong, Q.-G., & Blake, J. B. (2020). On phase space density and its radial gradient of outer radiation belt seed electrons: MMS/FEEPS observations. *Journal of Geophysical Research: Space Physics*, *125*(4), e2019JA027711. https://doi.org/10.1029/2019JA027711

Livadiotis, G., & McComas, D. J. (2013). Understanding kappa distributions: A toolbox for space science and astrophysics. *Space Science Reviews*, *175*(1–4), 183–214. https://doi.org/10.1007/s11214-013-9982-9

Loto'aniu, T. M., Redmon, R. J., Califf, S., Singer, H. J., Rowland, W., Macintyre, S., et al. (2019). The GOES-16 spacecraft science magnetometer. *Space Science Reviews*, *215*(4), 32. https://doi.org/10.1007/s11214-019-0600-3

Magnes, W., Hillenmaier, O., Auster, H.-U., Brown, P., Kraft, S., Seon, J., et al. (2020). Space weather magnetometer aboard GEO-KOMPSAT-2A. *Space Science Reviews*, *216*(8), 119. https://doi.org/10.1007/s11214-020-00742-2

Matzka, J., Stolle, C., Yamazaki, Y., Bronkalla, O., & Morschhauser, A. (2021). The geomagnetic *Kp* index and derived indices of geomagnetic activity. *Space Weather*, *19*(5), e2020SW002641. https://doi.org/10.1029/2020SW002641

Medeiros, C., Souza, V. M., Vieira, L. E. A., Sibeck, D. G., Halford, A. J., Kang, S.-B., et al. (2019). On the contribution of EMIC waves to the reconfiguration of the relativistic electron butterfly pitch angle distribution shape on 2014 September 12—A case study. *The Astrophysical Journal*, *872*(1), 36. https://doi.org/10.3847/1538-4357/aaf970

Millan, R. M., & Baker, D. N. (2012). Acceleration of particles to high energies in Earth's radiation belts. *Space Science Reviews*, *173*(1–4), 103–131. https://doi.org/10.1007/s11214-012-9941-x

Millan, R. M., & Thorne, R. M. (2007). Review of radiation belt relativistic electron losses. *Journal of Atmospheric and Solar-Terrestrial Physics*, *69*(3), 362–377. https://doi.org/10.1016/j.jastp.2006.06.019

Miyoshi, Y., Morioka, A., Misawa, H., Obara, T., Nagai, T., & Kasahara, Y. (2003). Rebuilding process of the outer radiation belt during the 3 November 1993 magnetic storm: NOAA and Exos-D observations. *Journal of Geophysical Research*, *108*(A1), 1004. https://doi.org/10.1029/2001JA007542

Morley, S. K., Henderson, M. G., Reeves, G. D., W. Friedel, R. H., & Baker, D. N. (2013). Phase space density matching of relativistic electrons using the van allen Probes: REPT results. *Geophysical Research Letters*, *40*(18), 4798–4802. https://doi.org/10.1002/grl.50909

Morley, S. K., Niehof, J. T., Welling, D. T., Larsen, B. A., Brunet, A., Engel, M. A., et al. (2024). *SpacePy* (version release-0.6.0) [Computer software]. *Zenodo*. https://doi.org/10.5281/zenodo.14268750

National Oceanic and Atmospheric Administration. (2010). National aeronautics and space administration, goddard space Flight center, and boeing satellite systems inc. In *GOES N Series Data Book (Rev D)*. Boeing Satellite Systems Inc. Retrieved from https://www.ngdc.noaa.gov/stp/satellite/goes/doc/GOES_N_Series_Databook_rev-D.pdf

Ni, B., Shprits, Y., Hartinger, M., Angelopoulos, V., Gu, X., & Larson, D. (2011). Analysis of radiation belt energetic electron phase space density using THEMIS SST measurements: Cross-satellite calibration and a case study: Themis SST cross-satellite calibration. *Journal of Geophysical Research*, *116*(A3), A03208. https://doi.org/10.1029/2010JA016104

Ni, B., Shprits, Y., Nagai, T., Thorne, R., Chen, Y., Kondrashov, D., & Kim, H. (2009). Reanalyses of the radiation belt electron phase space density using nearly equatorial CRRES and polar-orbiting Akebono satellite observations. *Journal of Geophysical Research*, *114*(A5), 2008JA013933. https://doi.org/10.1029/2008JA013933

Niehof, J. T., Morley, S. K., Welling, D. T., & Larsen, B. A. (2022). The SpacePy space science package at 12 years. *Frontiers in Astronomy and Space Sciences*, *9*, 1023612. https://doi.org/10.3389/fspas.2022.1023612

Olifer, L., Mann, I. R., Ozeke, L. G., Morley, S. K., & Louis, H. L. (2021). On the formation of phantom electron phase space density peaks in single spacecraft radiation belt data. *Geophysical Research Letters*, *48*(11), e2020GL092351. https://doi.org/10.1029/2020GL092351

21699402, 2025, 4, Downloaded from https://agupubs.onlinelibrary.wiley.com/doi/10.1029/2024JA033161, Wiley Online Library on [02/10/2025]. See the Terms and Conditions (https://onlinelibrary.wiley.com/terms-and-conditions) on Wiley Online Library for rules of use; OA articles are governed by the applicable Creative Commons License

Onsager, T. G., Chan, A. A., Fei, Y., Elkington, S. R., Green, J. C., & Singer, H. J. (2004). The radial gradient of relativistic electrons at geosynchronous orbit. *Journal of Geophysical Research*, *109*(A5), 2003JA010368. https://doi.org/10.1029/2003JA010368

Ozeke, L. G., Mann, I. R., Claudepierre, S. G., Henderson, M., Morley, S. K., Murphy, K. R., et al. (2019). The March 2015 superstorm revisited: Phase space density profiles and fast ULF wave diffusive transport. *Journal of Geophysical Research: Space Physics*, *124*(2), 1143–1156. https://doi.org/10.1029/2018JA026326

Pierrard, V., & Lazar, M. (2010). Kappa distributions: Theory and applications in space plasmas. *Solar Physics*, *267*(1), 153–174. https://doi.org/10.1007/s11207-010-9640-2

Rich, F. J., Califf, S., Loto'aniu, P. T. M., Coakley, M., Krimchansky, A., & Singer, H. J. (2024). Intersatellite comparisons of GOES magnetic field measurements. *Space Weather*, *22*(5), e2023SW003736. https://doi.org/10.1029/2023SW003736

Ripoll, J.-F., Claudepierre, S. G., Ukhorskiy, A. Y., Colpitts, C., Li, X., Fennell, J. F., & Crabtree, C. (2020). Particle dynamics in the Earth's radiation belts: Review of current research and open questions. *Journal of Geophysical Research: Space Physics*, *125*(5), e2019JA026735. https://doi.org/10.1029/2019JA026735

Roederer, J. G. (1970). Dynamics of geomagnetically trapped radiation. In *Physics and Chemistry in space* (Vol. 2). Springer Berlin Heidelberg. https://doi.org/10.1007/978-3-642-49300-3

Roederer, J. G., & Lejosne, S. (2018). Coordinates for representing radiation belt particle flux. *Journal of Geophysical Research: Space Physics*, *123*(2), 1381–1387. https://doi.org/10.1002/2017JA025053

Roederer, J. G., & Zhang, H. (2014). Dynamics of magnetically trapped particles: Foundations of the physics of radiation belts and space plasmas. In *Astrophysics and space science library* (Vol. 403). Springer Berlin, Heidelberg. https://doi.org/10.1007/978-3-642-41530-2

Sarris, T. E., Li, X., Zhao, H., Khoo, L. Y., Liu, W., & Temerin, M. A. (2021). On the association between electron flux Oscillations and local phase space density gradients. *Journal of Geophysical Research: Space Physics*, *126*(2), e2020JA028891. https://doi.org/10.1029/2020JA028891

Schiller, Q., Li, X., Blum, L., Tu, W., Turner, D. L., & Blake, J. B. (2014). A nonstorm time enhancement of relativistic electrons in the outer radiation belt. *Geophysical Research Letters*, *41*(1), 7–12. https://doi.org/10.1002/2013GL058485

Schulz, M., & Lanzerotti, L. J. (1974). Particle diffusion in the radiation belts. In *Physics and Chemistry in Space* (Vol. 7). Springer Berlin Heidelberg. https://doi.org/10.1007/978-3-642-65675-0

Selesnick, R. S., & Blake, J. B. (2000). On the source location of radiation belt relativistic electrons. *Journal of Geophysical Research*, *105*(A2), 2607–2624. https://doi.org/10.1029/1999JA900445

Seol, W.-H., Lee, C.-H., Seon, J., Shin, Y.-C., Kim, K.-H., Larson, D. E., et al. (2023). Estimation of geometric factors for the particle detecting instruments of the geostationary satellite GK2A at 128.2°E longitude based on observations of the outer radiation belt during geomagnetically quiet periods. *Space Weather*, *21*(1), e2022SW003265. https://doi.org/10.1029/2022SW003265

Seon, J., Chae, K.-S., Na, G. W., Seo, H.-K., Shin, Y.-C., Woo, J., et al. (2020). Particle detector (PD) experiment of the Korea space environment monitor (KSEM) aboard geostationary satellite GK2A. *Space Science Reviews*, *216*(1), 13. https://doi.org/10.1007/s11214-020-0636-4

Shprits, Y., Daae, M., & Ni, B. (2012). Statistical analysis of phase space density buildups and dropouts. *Journal of Geophysical Research*, *117*(A1), 2011JA016939. https://doi.org/10.1029/2011JA016939

Shprits, Y., Kondrashov, D., Chen, Y., Thorne, R., Ghil, M., Friedel, R., & Reeves, G. (2007). Reanalysis of relativistic radiation belt electron fluxes using CRRES satellite data, a radial diffusion model, and a Kalman filter. *Journal of Geophysical Research*, *112*(A12), 2007JA012579. https://doi.org/10.1029/2007JA012579

Shprits, Y. Y., Subbotin, D., & Ni, B. (2009). Evolution of electron fluxes in the outer radiation belt computed with the VERB code. *Journal of Geophysical Research*, *114*(A11), 2008JA013784. https://doi.org/10.1029/2008JA013784

Shue, J.-H., Song, P., Russell, C. T., Steinberg, J. T., Chao, J. K., Zastenker, G., et al. (1998). Magnetopause location under extreme solar wind conditions. *Journal of Geophysical Research*, *103*(A8), 17691–17700. https://doi.org/10.1029/98JA01103

Sibeck, D. G., McEntire, R. W., Lui, A. T. Y., Lopez, R. E., & Krimigis, S. M. (1987). Magnetic field drift shell splitting: Cause of unusual dayside particle pitch angle distributions during storms and substorms. *Journal of Geophysical Research*, *92*(A12), 13485–13497. https://doi.org/10.1029/JA092iA12p13485

Su, Z., Xiao, F., Zheng, H., & Wang, S. (2010). Combined radial diffusion and adiabatic transport of radiation belt electrons with arbitrary pitch angles. *Journal of Geophysical Research*, *115*(A10), 2010JA015903. https://doi.org/10.1029/2010JA015903

Szabó-Roberts, M., Shprits, Y. Y., Allison, H. J., Vasile, R., Smirnov, A. G., Aseev, N. A., et al. (2021). Preliminary statistical comparisons of spin-averaged electron data from arase and van allen Probes instruments. *Journal of Geophysical Research: Space Physics*, *126*(7), e2020JA028929. https://doi.org/10.1029/2020JA028929

Taylor, M. G. G. T., Friedel, R. H. W., Reeves, G. D., Dunlop, M. W., Fritz, T. A., Daly, P. W., & Balogh, A. (2004). Multisatellite measurements of electron phase space density gradients in the Earth's inner and outer magnetosphere. *Journal of Geophysical Research*, *109*(A5), 2003JA010294. https://doi.org/10.1029/2003JA010294

Tsyganenko, N. A., & Sitnov, M. I. (2005). Modeling the dynamics of the inner magnetosphere during strong geomagnetic storms. *Journal of Geophysical Research*, *110*(A3), 2004JA010798. https://doi.org/10.1029/2004JA010798

Turner, D. L., Angelopoulos, V., Li, W., Bortnik, J., Ni, B., Ma, Q., et al. (2014). Competing source and loss mechanisms due to wave-particle interactions in Earth's outer radiation belt during the 30 September to 3 October 2012 geomagnetic storm. *Journal of Geophysical Research: Space Physics*, *119*(3), 1960–1979. https://doi.org/10.1002/2014JA019770

Turner, D. L., Angelopoulos, V., Shprits, Y., Kellerman, A., Cruce, P., & Larson, D. (2012). Radial distributions of equatorial phase space density for outer radiation belt electrons. *Geophysical Research Letters*, *39*(9), 2012GL051722. https://doi.org/10.1029/2012GL051722

Turner, D. L., & Li, X. (2008). Radial gradients of phase space density of the outer radiation belt electrons prior to sudden solar wind pressure enhancements. *Geophysical Research Letters*, *35*(18), 2008GL034866. https://doi.org/10.1029/2008GL034866

Turner, D. L., Morley, S. K., Miyoshi, Y., Ni, B., & Huang, C.-L. (2013). Outer radiation belt flux dropouts: Current understanding and unresolved questions. In D. Summers, I. R. Mann, D. N. Baker, & M. Schulz (Eds.), *Geophysical Monograph series* (pp. 195–212). American Geophysical Union. https://doi.org/10.1029/2012GM001310

Vampola, A. L. (1997). Outer zone energetic electron environment update. In *Conference on the high Energy Radiation Background in Space* (pp. 128–136). Workshop Record. https://doi.org/10.1109/CHERBS.1997.660263

Van Allen, J. A., Baker, D. N., Randall, B. A., & Sentman, D. D. (1974). The magnetosphere of jupiter as observed with pioneer 10: 1. Instrument and principal findings. *Journal of Geophysical Research*, *79*(25), 3559–3577. https://doi.org/10.1029/JA079i025p03559

Wang, C., Zhang, X., Li, J., Huang, C., Zhang, X., Jing, T., et al. (2013). Cross-calibration of high energetic particles data—A case study between FY-3B and NOAA-17. *Science China Technological Sciences*, *56*(11), 2668–2674. https://doi.org/10.1007/s11431-013-5375-2

West, H. I., Buck, R. M., & Walton, J. R. (1973). Electron pitch angle distributions throughout the magnetosphere as observed on Ogo 5. *Journal of Geophysical Research*, *78*(7), 1064–1081. https://doi.org/10.1029/JA078i007p01064

21699402, 2025, 4, Downloaded from https://agupubs.onlinelibrary.wiley.com/doi/10.1029/2024JA033161, Wiley Online Library on [02/10/2025]. See the Terms and Conditions (https://onlinelibrary.wiley.com/terms-and-conditions) on Wiley Online Library for rules of use; OA articles are governed by the applicable Creative Commons License

Whittaker, I. C., Gamble, R. J., Rodger, C. J., Clilverd, M. A., & Sauvaud, J. (2013). Determining the spectra of radiation belt electron losses: Fitting DEMETER electron flux observations for typical and storm times. *Journal of Geophysical Research: Space Physics*, *118*(12), 7611–7623. https://doi.org/10.1002/2013JA019228

Woo, J., Seol, W., Chae, K., Lee, J., Lee, E., & Seon, J. (2020). Charging monitor aboard the geostationary satellite GK2A at 128.2° E longitude. *IEEE Transactions on Nuclear Science*, *67*(4), 740–745. https://doi.org/10.1109/TNS.2020.2977473

Xiao, F., Chen, L., & Li, J. (2008). Energetic particles modeled by a generalized relativistic kappa-type distribution function in plasmas. *Plasma Physics and Controlled Fusion*, *50*(10), 105002. https://doi.org/10.1088/0741-3335/50/10/105002

Xiao, F., Yang, C., Su, Z., Zhou, Q., He, Z., He, Y., et al. (2015). Wave-driven butterfly distribution of Van Allen belt relativistic electrons. *Nature Communications*, *6*(1), 8590. https://doi.org/10.1038/ncomms9590

Zhang, Y., Ni, B., Xiang, Z., Zhang, X., Zhang, X., Gu, X., et al. (2018). Inter-satellite calibration of FengYun 3 medium energy electron fluxes with POES electron measurements. *Advances in Space Research*, *61*(9), 2290–2300. https://doi.org/10.1016/j.asr.2018.02.017

Zhao, H., Johnston, W. R., Baker, D. N., Li, X., Ni, B., Jaynes, A. N., et al. (2019). Characterization and evolution of radiation belt electron energy spectra based on the van allen Probes measurements. *Journal of Geophysical Research: Space Physics*, *124*(6), 4217–4232. https://doi.org/10.1029/2019JA026697

Zhao, H., Ni, B., Li, X., Baker, D. N., Johnston, W. R., Zhang, W., et al. (2019b). Plasmaspheric hiss waves generate a reversed energy spectrum of radiation belt electrons. *Nature Physics*, *15*(4), 367–372. https://doi.org/10.1038/s41567-018-0391-6

Zhu, C., Zhang, X., Zhang, H., Li, X., Zong, W., Li, J., et al. (2022). Inter-calibration between the electron flux measurements of FengYun-3B and van allen probe-A based on electron phase space density conjunctions. *Journal of Geophysical Research: Space Physics*, *127*(9), e2022JA030463. https://doi.org/10.1029/2022JA030463

21699402, 2025, 4, Downloaded from https://agupubs.onlinelibrary.wiley.com/doi/10.1029/2024JA033161, Wiley Online Library on [02/10/2025]. See the Terms and Conditions (https://onlinelibrary.wiley.com/terms-and-conditions) on Wiley Online Library for rules of use; OA articles are governed by the applicable Creative Commons License